A Depth-Derived Pleistocene Age-Model: Uncertainty Estimates, Sedimentation Variability, and Nonlinear Climate Change

A depth-derived Pleistocene age model: Uncertainty estimates, sedimentation variability, and nonlinear climate change

Peter Huybers and Carl Wunsch

Program in Atmospheres, Oceans, and Climate, Massachusetts Institute of Technology, Cambridge, Massachusetts, USA

Received 30 October 2002; revised 3 December 2003; accepted 2 February 2004; published 27 March 2004.

[1] A new chronology of glaciation, spanning the last 780,000 years, is estimated from 21 marine sediment cores using depth as a proxy for time. To avoid biasing this ''depth-derived'' age estimate, the depth scale is first corrected for the effects of sediment compaction. To provide age uncertainty estimates, the spatial and temporal variability of marine sediment accumulation rates are estimated and modeled as an autocorrelated stochastic process. Depth-derived ages are estimated to be accurate to within ±9000 years, and within this uncertainty are consistent with the orbitally tuned age estimates. Nonetheless, the remaining differences between the depth and orbitally tuned chronologies produce important differences in the spectral domain. From the $\delta^{18}O$ record, using the depth-derived ages, we infer that there are weak nonlinearities involving the 100 kyr and obliquity frequency bands which generate interaction bands at sum and difference frequencies. If an orbitally tuned age model is instead applied, these interactions are suppressed, with the system appearing more nearly linear. *INDEX TERMS:* 1620 Global Change: Climate dynamics (3309); 1869 Hydrology: Stochastic processes; 3005 Marine Geology and Geophysics: Geomagnetism (1550); 3220 Mathematical Geophysics: Nonlinear dynamics; 4267 Oceanography: General: Paleoceanography; *KEYWORDS:* tuning, sediment accumulation, nonlinear

Citation: Huybers, P., and C. Wunsch (2004), A depth-derived Pleistocene age model: Uncertainty estimates, sedimentation variability, and nonlinear climate change, *Paleoceanography*, *19*, PA1028, doi:10.1029/2002PA000857.

1. Introduction

[2] Inference concerning past climate change relies heavily upon the assignment of ages to measurements and events recorded in marine and ice cores as well as to a variety of isolated markers in the geological record. Sedimentation and snow accumulation are analogous to strip-chart recorders, marking the past climate state in a large variety of physical variables. These records tend to be noisy and blurred by bioturbation and a variety of diffusive-like processes, [e.g., *Pestiaux and Berger*, 1984]. The major difficulty however, is that these strip-chart recorders run at irregular rates, stop completely, or even rewind and erase previous sections. If depth is taken as a simple proxy for time, irregularities in sedimentation stretch and squeeze the apparent timescale, and so distort the signals being sought. To the degree that the changes in rates are proportional to the signals themselves, one has a challenging signal demodulation problem. It is not an exaggeration to say that understanding and removing these age-depth (or age model) errors is one of the most important of all problems facing the paleoclimate community. Timing accuracy is crucial to understanding the nature of climate variability and the underlying cause and effect. Here we attempt to understand the nature of some of these age model errors, and to then apply that insight to construct a timescale for marine sediment cores spanning the last 780,000 years.

[3] The currently favored method for estimating Pleistocene age is orbital tuning [e.g., *Imbrie et al.*, 1984; *Martinson et al.*, 1987; *Shackleton et al.*, 1990] wherein a constant phase relationship is assumed between paleoclimatic measurements and an insolation forcing based on Milankovitch theory [*Milankovitch*, 1941]. One of the well-known successes of orbital tuning was the *Johnson* [1982], and later *Shackleton et al.* [1990], prediction of a Brunhes-Matuyama magnetic reversal (B-M) age older than previously estimated, an inference which was subsequently confirmed by argon-argon dating [e.g., *Singer and Pringle*, 1996]. A number of radiometric dates for termination 2 also support the orbital age model [e.g., *Broecker et al.*, 1968].

[4] Milankovitch theory, however, has come under question [e.g., *Karner and Muller*, 2000; *Elkibbi and Rial*, 2001; *Wunsch*, 2003a] and radiometric ages conflicting with the orbital ages have also been reported: for termination 2 by *Henderson and Slowey* [2000], and *Gallup et al.* [2002]; for terminations 3 by *Karner and Marra* [1998]; and for a variety of events by *Winograd et al.* [1992], among others. To understand long term climate change, it is necessary to resolve these conflicting age estimates. To avoid circular reasoning, an age model devoid of orbital assumptions is needed.

[5] As suggested by *Shaw* [1964], the age of geological events identifiable in multiple stratigraphies may be estimated using mean sediment accumulation rates, here termed ''depth-derived'' ages. The literature has numerous examples of depth-derived ages (e.g., *Shackleton and Opdyke* [1972], from 900 to 0 kyr BP; *Hays et al.* [1976], 500–0 kyr BP; *Williams et al.* [1988], 1900–0 kyr BP; *Martinson et al.* [1987], 300–0 kyr BP; and *Raymo* [1997], 800–0 kyr BP), but whose results have been inconclusive. The most comprehensive existing study, that by *Raymo* [1997], used

0883-8305/04/2002PA000857$12.00

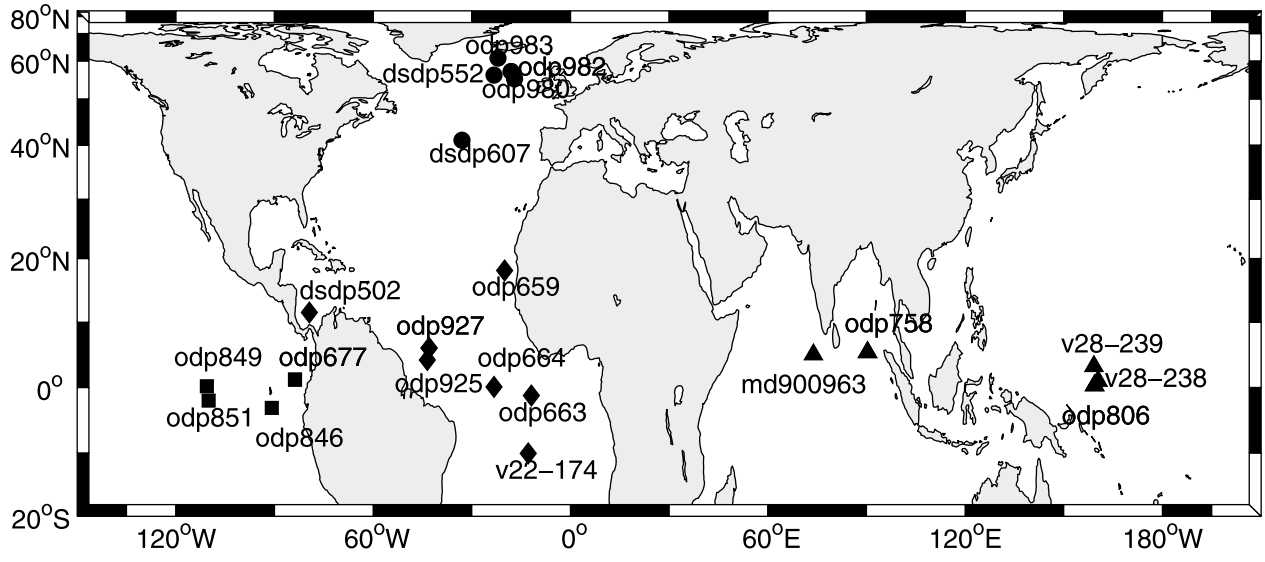

Figure 1. The locations of the records used in this study. Markings indicate geographic groupings: the North Atlantic (circles), Indian and western equatorial Pacific (triangles), equatorial Atlantic (diamonds), and eastern equatorial Pacific Oceans (squares).

11 marine sediment cores. Owing to her inference of systematic core extension during recovery, she could not distinguish between the conflicting orbital and radiometric termination 2 age estimates.

[6] This present study extends the depth-derived approach to 21 sediment cores, described below and, in what is a critical factor, accounts for the down-core trend in sediment compaction. An age uncertainty estimate for the depth-derived age model is provided, in part, by modeling accumulation rate variability as an autocorrelated stochastic process. Within the estimated uncertainty, the depth-derived and orbital age models are consistent with one another, but the depth-derived age model implies nonlinear relationships between earth's orbital variations and the δ^{18}O climate proxy that are absent when the orbital age models are applied.

2. Data

[7] An ensemble of 26 δ^{18}O records from 21 separate coring sites are used in this study. The core sites are shown in Figure 1 and can be divided into four geographical regions: the North Atlantic, eastern equatorial Pacific, equatorial Atlantic, and the Indian and western equatorial Pacific Oceans. Core site locations heavily favor the Northern Hemisphere. Four of the records are from piston cores (V22-174, V28-238, V28-239, and MD900963) while the remainder are composite records spliced together from multiple cores recovered by the Deep Sea Drilling Program (DSDP) or Ocean Drilling Program (ODP). For ODP and DSDP sites, the composite depth scale or, if available, the ODP revised composite depth scale, is used. Table 1 lists the pertinent statistics and gives references for each core.

[8] All δ^{18}O records that were available to us, believed to be stratigraphically intact, and which extend through the B-M were included in this study. Use of planktic records, in addition to the benthic, allows for the inclusion of seven more sediment cores and decreases the uncertainty associated with the depth-derived age model. The depth of the B-M was reported in the literature as identifiable via magnetic stratigraphy in 12 of the 21 cores, and these cores are indicated by an "M" appended to the name in Table 1. For the δ^{18}O records associated with these 12 cores, the B-M invariably occurs within δ^{18}O stage 19. Where the B-M transition is not identifiable, the depth of event 19.1, the most negative δ^{18}O value in stage 19, is instead used, and in all cases an age of 780 kiloyears before present (kyr BP) (*Singer and Pringle* [1996], rounded to the nearest ten kyr) is assigned.

[9] At the outset, it is convenient to correct for the effects of compaction on the depth scale. Sediment compaction typically increases with depth [e.g., *Bahr et al.*, 2001] and thus systematically compresses a greater quantity of time into a given depth interval. Assuming that the estimated trends in porosity reflect inhomogeneities in relative compaction, we apply a correction based on conservation of dry sediment volume wherein the thickness of each sediment layer is adjusted so as to remove trends in porosity. Porosity trends are estimated by fitting a low-order polynomial to porosity observations; for cores without observed porosity profiles, comprising 13 of the 21 cores, the mean down-core porosity trend from the observed porosity profiles is instead used. While this method introduces an age model uncertainty of up to ±6 kyr, the alternative is an expected age model bias of up to 15 kyr. See Appendix A for more details. All subsequent depth references are to this decompacted scale. Note *Huybers* [2002] did not adequately account for the effects of compaction and thus arrived at older age estimates.

Table 1. Characteristics and Primary References for Each Core[a]

Name	Reference	Species	S	Δt	Water Depth	Latitude	Longitude
DSDP502T	*Prell* [1982]	P	1.9	6.5	3052	12N	79E
DSDP552MT	*Shackleton and Hall* [1984]	B	1.9	6.4	2301	56N	23W
DSDP607MT	*Ruddiman et al.* [1989]	B	4.0	3.5	3427	41N	33W
MD900963M	*Bassinot et al.* [1994]	P	4.6	2.3	2446	5N	74E
ODP659M	*Tiedemann et al.* [1994]	B	3.1	3.9	3070	18N	21W
ODP663	*de Menocal et al.* [1993]	P	3.9	3.0	3706	1S	12W
ODP664M	*Raymo* [1997]	B	3.7	3.4	3806	0	23W
ODP677MT	*Shackleton et al.* [1990]	B,P	3.9	2.1,1.8	3461	1N	84W
ODP758MT	*Chen et al.* [1995]	B,P	1.6	6.5,6.7	2924	5N	90E
ODP806T	*Berger et al.* [1994]	B,P	2.0	4.8	2520	0	159E
ODP846MT	*Mix et al.* [1995a]	B	3.7	2.5	3461	3S	91W
ODP849MT	*Mix et al.* [1995b]	B	2.9	3.6	3296	0	111W
ODP851MT	*Ravelo and Shackleton* [1995]	P	2.0	5.0	3760	2S	110W
ODP925	*Bickert et al.* [1997] *Curry and Cullen* [1997]	B	3.7	2.2	3041	4N	43W
ODP927T	*Cullen and Curry* [1997] *Curry and Cullen* [1997]	B,P	4.5	3.2,2.2	3315	6N	43W
ODP980T	*Flower* [1999] *McManus et al.* [1999, 2002] *Oppo et al.* [1998, 2001]	B	12.3	1.6	2169	55N	17W
ODP982T	*Venz et al.* [1999]	B,P	2.5	2.3, 2.0	1134	57N	18W
ODP983	*Channell et al.* [1997] *McManus et al.* [2003]	B	11.4	0.9	1983	61N	22W
V22-174	*Thierstein et al.* [1977]	P	1.8	5.3	2630	10S	13W
V28-238MT	*Shackleton and Opdyke* [1976]	P	1.5	5.5	3120	1N	160E
V28-239M	*Shackleton and Opdyke* [1976]	P	0.9	5.6	3490	3N	159E

[a]An "M" appended to the core name indicates that the B-M was identified via magnetic susceptibility measurements, and a "T" indicates the availability of a published orbitally tuned age model. Columns from left to right display δ^{18}O species benthic (B) and/or planktic (P), the mean sediment accumulation rate ($\bar{S}$, cm/kyr), the mean interval between δ^{18}O measurements (Δt, kyr), water depth (meters), and the latitude and longitude of each core site.

[10] It is helpful to define some terminology used in estimating the depth-derived age model. An "event" is a δ^{18}O feature whose depth can be uniquely identified within each δ^{18}O record. When an age is fixed to an event, it becomes an age control point (ACP). Two types of events are referred to, "stages" and "terminations." Stages are defined as local minima or maxima in the δ^{18}O record [*Prell et al.*, 1986] where the numbering system suggested by *Imbrie et al.* [1984] is used. All the stages referred to in this study have odd numbers after the decimal point, corresponding to low ice volume excursions in the δ^{18}O record. Terminations are defined as an abrupt shift from glacial to interglacial conditions [*Broecker*, 1984], where the assigned depth is the midpoint between the local δ^{18}O minimum and maximum. Figure 2 shows the eight termination midpoints and nine stages which were visually identified in each δ^{18}O record. For comparison purposes, Figure 2 also shows these seventeen events identified on the SPECMAP δ^{18}O stack [*Imbrie et al.*, 1984].

[11] A second, more objective, method of event correlation was also implemented using an automated cross-correlation maximization procedure. Within an expected error of 1 kyr, this algorithm, termed XCM, yielded event correlations which were identical to those determined from the visual procedure. This result gives some confidence in the ability to relate events in different δ^{18}O records. For more detail, see Appendix B and *Huybers* [2002].

[12] The choice of seventeen ACPs reflects a minimalist strategy for constraining the $\delta^{18}O$ record, especially when compared with the SPECMAP δ^{18}O stack which uses five times as many ACPs in the same 770 kyr interval. We do not use more ACPs for three reasons: (1) only a small decrease in age model uncertainty would result (section 4.1); (2) while more high-frequency structure in the composite δ^{18}O record is expected to be retained, false structure could be built into the averaged record by aligning noisy features; and (3) more ACPs are not expected to aid in resolving the spectra of higher-frequency processes because of the spectral smearing due to age model uncertainty (section 5.1).

3. Time and Sediment Accumulation

3.1. A Random Walk Model

[13] To understand the relationships between age and depth, we need a model of sediment accumulation rates. Both are expected to have systematic and stochastic elements, the latter here modeled as a random walk. Let d_n be the depth of a layer of sediment in a core at time step n. Then for a unit time step, Δt, d_n increases as

$$d_{n+1} = d_n + \Delta t\bar{S} + \Delta t S'_n + W_n, \tag{1}$$

where $\bar{S}$ is the mean sediment accumulation rate, S'_n is the zero-mean stochastic contribution, and W_n is a systematic term. Dividing by $\bar{S}$ converts the change in depth for each increment to a true time increment plus two anomaly terms,

$$t'_{n+1} = t'_n + \Delta t + \Delta t\frac{S'_n}{\bar{S}} + \frac{W_n}{\bar{S}}, \tag{2}$$

where $t'_n = d_n/S$, is the linear age estimate. W_n is treated here primarily as the sediment compaction affect (see

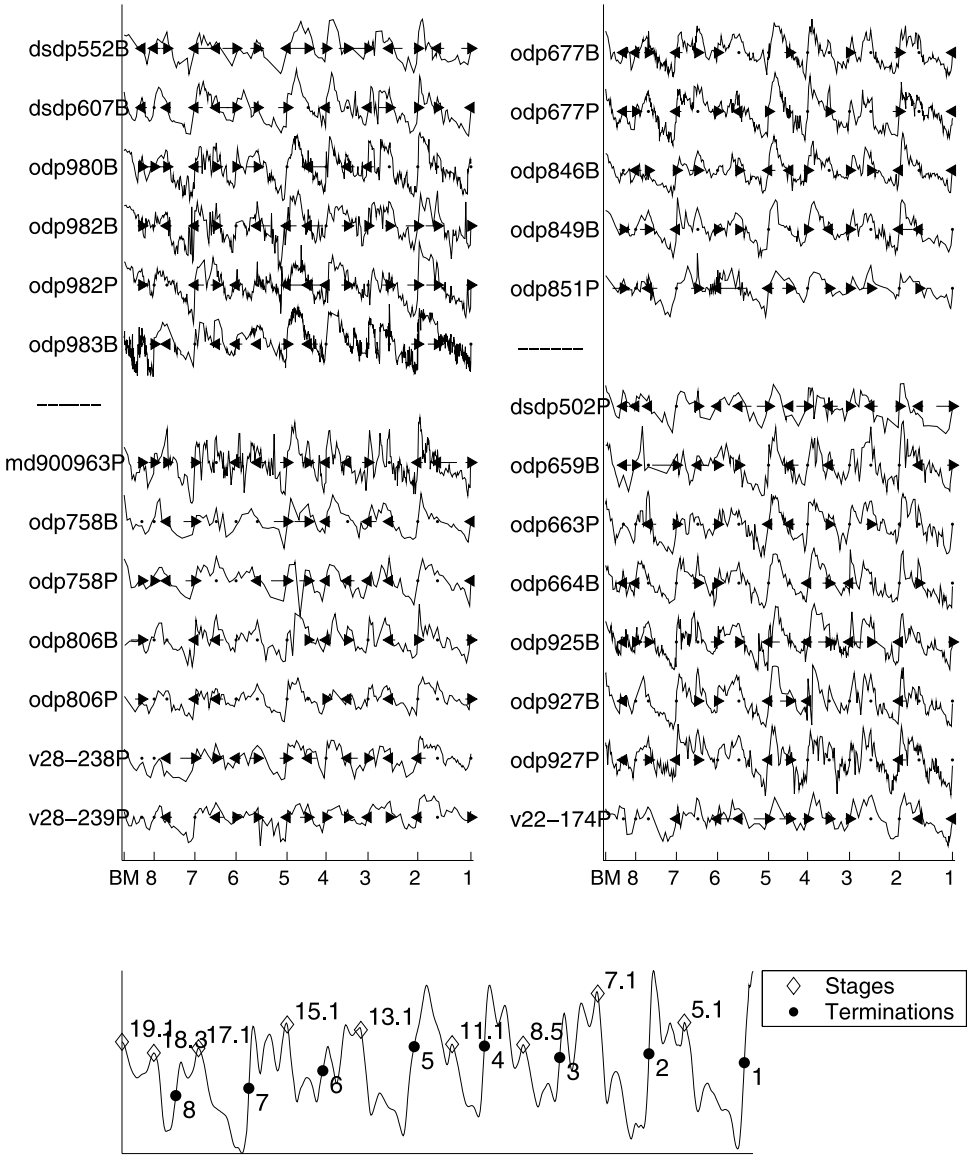

Figure 2. The $\delta^{18}O$ isotope records, grouped into the four geographic categories shown in Figure 1: the North Atlantic (top left), eastern equatorial Pacific (top right), Indian and western equatorial Pacific (bottom left), and equatorial Atlantic Oceans (bottom right). As described in the text, simultaneity between all records is enforced at 17 isotopic events. The ordinate is labeled with the B-M boundary location and termination numbers. The abscissa is to scale, and the $\delta^{18}O$ records are vertically off-set from one another. The arrows at each event indicate how the age model was adjusted from a linear age-depth relationship beginning with stage 18.3 and working toward stage 5.1. The letters B and P are appended to the record name to indicate it as benthic or planktic. The bottom panel is the SPECMAP $\delta^{18}O$ stack oriented such that upward indicates lighter $\delta^{18}O$ (interglacial). The SPECMAP stack is labeled with each of the 17 events for which ages are later estimated and the ordinate is arbitrary. Note that in this paper, time always increases to the right.

Appendix A) although long-term variation in bioproductivity, terrigenous discharge, dust transport, and coring artifacts are also implicated. We focus first on the random element.

[14] The simplest case is when S'_n is a white noise process, $\langle S'_n S'_m \rangle = 0$, $n \neq m$ (brackets, $\langle \cdot \rangle$, denote an ensemble average) and the variance of the difference between the apparent and true time grows linearly on average [*Feller*, 1966],

$$\left\langle \left(t'_n - n\Delta t\right)^2 \right\rangle = n\Delta t \frac{\sigma^2}{\bar{S}^2}. \tag{3}$$

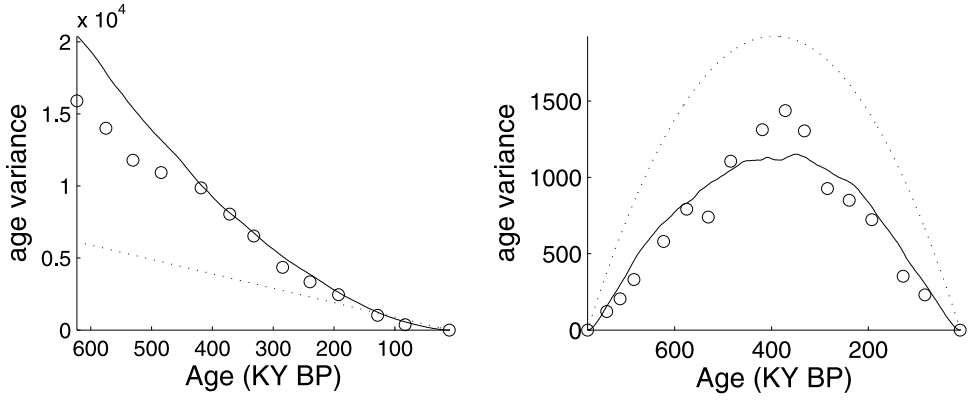

Figure 3. The age variance from the observations (circles) and from the simple models using correlated (solid line) and uncorrelated (dotted lines) sediment accumulation rates. Both the one ACP (left) and two ACP (right) cases are shown with a simple random walk using $J = 10$ and a correlated random walk using $J = 0.5$ and $s_o = 1/40$. The simple random walk respectively under- and over-estimates the age variance, while the correlated random walk is similar to the observational variance.

where $\sigma^2 = \langle S_n'^2 \rangle$. Following *Moore and Thomson* [1991] and *Wunsch* [2000], we term the variance growth rate the "jitter,"

$$J = \left(\frac{\sigma}{\bar{S}}\right)^2, \tag{4}$$

an appropriate measure when only one $\delta^{18}O$ event is constrained to a known age. If the duration of the temporal random walk is fixed by introducing a second ACP at $t = N\Delta t$, the expected variance between the two fixed points behaves as a "Brownian bridge" process. Following *Odell* [1975] and *Bhattacharya and Waymire* [1990], the Brownian bridge analogue of equation (3) is

$$\left\langle \left(t_n' - n\Delta t\right)^2 \right\rangle = n\Delta t J\left(1 - \frac{n}{N}\right), \quad 0 \le n \le N, \tag{5}$$

where N is the total number of time steps between the 2 ACPs. Age variance is then zero at the two end points, with a maximum at the midpoint. Integrating, and comparing equations (3) and (5), shows that the inclusion of a second ACP results in a three-fold reduction in mean age variance.

3.2. Determining the Stochastic Element

[15] To estimate the character and degree of jitter in deep sea sediment cores, it is useful to construct some simple age models. Rather than using the mixed stage and termination notation, each event is assigned a number, $1 \le k \le 17$, running in temporal sequence from termination 1 to stage 19.1. Mean accumulation rates in core j between events 17 (stage 19.1) and 13 (termination 7) can be estimated as

$$\bar{S}_j^{(1)} = \frac{d_{j,17} - d_{j,13}}{160}, \tag{6}$$

where $d_{j,k}$ is the depth of event k, and 160 kyr is roughly the duration between events 17 and 13. If event 1 is pinned to an age of 10.6 kyr before present (BP), the ages of events 1 through 13 are then estimated as

$$A_{j,k}^{(1)} = \frac{d_{j,k} - d_{j,1}}{\bar{S}_j^{(1)}} + 10.6, \quad 1 \le k \le 13, \tag{7}$$

where the superscript indicates the use of one ACP. If a second ACP at the B-M transition is incorporated, an age model may be expressed as

$$\begin{aligned} \bar{S}_j^{(2)} &= \frac{d_{j,17} - d_{j,1}}{780 - 10.6}, \\ A_{j,k}^{(2)} &= \frac{d_{j,k} - d_{j,1}}{\bar{S}_j^{(2)}} + 10.6, \quad 1 \le k \le 17, \end{aligned} \tag{8}$$

where 780 kyr BP is the age of B-M transition.

[16] Calculation of the variance in age estimates for each event permits comparison with the random walk models of sediment accumulation. First, the mean age of each event is determined by averaging over all cores,

$$\bar{A}_k^{(i)} = \frac{1}{21}\sum_{j=1}^{21} A_{j,k}^{(i)}, \tag{9}$$

for both the $i = 1$ and $i = 2$ ACP cases. When planktic and benthic $\delta^{18}O$ records are available within the same core, only the benthic record is used. The age variance can then be estimated as

$$v_k^{(i)} = \frac{1}{20}\sum_{j=1}^{21}\left(A_{j,k}^{(i)} - \bar{A}_k^{(i)}\right)^2, \quad 1 \le k \le 17. \tag{10}$$

[17] Figure 3 shows the calculated age variances, $v_k^{(i)}$ with $i = \{1, 2\}$. As expected, $v_k^{(1)}$ increases with the elapsed time from event one, t, and $v_k^{(2)}$ has a Brownian bridge character.

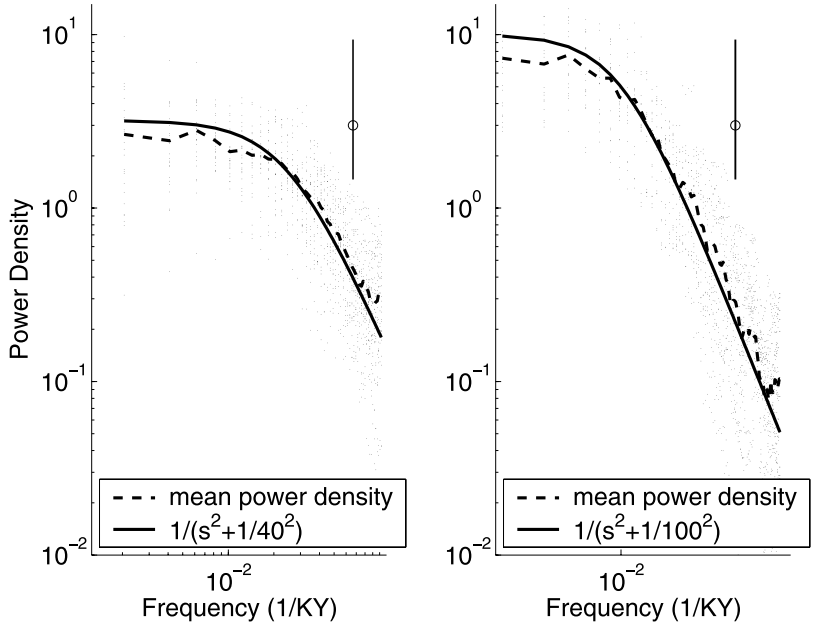

Figure 4. The multitaper spectral estimate of sediment accumulation rates for each record (dots), the mean from all the spectral estimates (dashed line), and an approximate spectral fit (solid line). Left panel is the analysis using the Devils Hole age model, and the right panel is from the orbital age models. Vertical bars indicate the approximate 95% confidence interval for the estimates from individual records (dots).

Also shown are the simple random walk and Brownian bridge models as determined from equations (3) and (5) with $J = 10$ in both cases. Were the model adequate, a single value of the jitter should be applicable to modeling both $v_k^{(1)}$ and $v_k^{(2)}$, but it is evident from Figure 3 that $J = 10$ underestimates the variance of $v^{(1)}$ and over-estimates that of $v^{(2)}$. Equation (3) also predicts $v_k^{(1)}$ is proportional to t, but it appears more nearly proportional to t^2 and is thus inconsistent with the hypothesis of a simple random walk in sediment accumulation. Some other effect is required to explain the result.

3.3. Sediment Accumulation With Autocovariance

[18] A generalization of the simple random walk to a correlated random walk is capable of accounting for the observed quadratic growth in the $v^{(1)}$ age variance. This generalization is plausible because sediment accumulation rates are themselves climate variables and can be expected to have a structured frequency spectrum implying temporal autocorrelation. To proceed, it is first necessary to adopt an age model estimated independent of accumulation rates.

[19] The Devils Hole record is devoid of orbital assumptions [*Winograd et al.*, 1992] and has a radiometric age model with uncertainties ranging from ±10 kyr at its oldest time, 519 kyr BP, to ±2 kyr at its youngest, 140 kyr BP. A complication, however, is that the Devils Hole record is, in places, offset from the marine δ^{18}O by up to 10 to 15 kyr and is thus not suitable for directly dating the marine δ^{18}O records [*Winograd et al.*, 1997; *Herbert et al.*, 2001]. In estimating marine sediment accumulation rates, only the duration between events needs to be equal, and we assume that the relative timing between the marine and Devils Hole δ^{18}O records is constant during most intervals. Acknowledging that this fixed-lag assumption probably breaks down during glacial maxima and terminations, the marine $A^{(2)}$ age models are nonetheless adjusted to maximize the squared zero-lag cross-correlation between the marine and Devils Hole δ^{18}O records using the XCM algorithm (see Appendix B). The derivative of depth relative the adjusted $A^{(2)}$ age models then provide estimates of accumulation rates.

[20] For the purpose of comparison, accumulation rates were also estimated from the orbitally derived age models provided by other authors, as indicated in Table 1. Figure 4 shows the power density spectral estimates of sediment accumulation rates using the multitaper method [*Thomson*, 1990] with both the Devils Hole and the published orbital age models. Both spectra may be characterized as

$$\Phi(s, s_0) = \frac{1}{s^2 + s_o^2}, \tag{11}$$

where Φ is the power density and s the frequency. Such a relationship is consistent with an autoregressive process of order 1 (AR(1)), and implies a minus two power law relationship for frequencies above s_o, with white noise at the lowest frequencies. The Devils Hole age model gives $s_o \approx 1/40$ kyr, but the orbital age models are consistent with the result of *Mix et al.* [1995b] with $s_o \approx 1/100$ kyr. This difference in shape is likely due to errors in one or both of the age models. The scope of the spectral damage owing to jitter is unclear, but as discussed later, either value of s_o gives a parameterization of accumulation rate variations consistent with the observed $v^{(1)}$ and $v^{(2)}$ age variances.

Table 2. $A^{(2)}$ Age Estimate (kyr BP) for Each Event in Each $\delta^{18}O$ Record, and the Mean Age of Each Event Along With Its Estimated Uncertainty (±kyr)[a]

	Event (Associated Stage/Termination)																
	17 (19.1)	16 (18.3)	15 (VIII)	14 (17.1)	13 (VII)	12 (15.1)	11 (VI)	10 (13.11)	9 (V)	8 (11.1)	7 (IV)	6 (8.5)	5 (III)	4 (7.1)	3 (II)	2 (5.1)	1 (I)
dsdp502P	780	730	695	660	601	560	510	435	395	342	327	260	220	157	102	49	11
dsdp552B	780	734	693	677	576	519	505	474	362	321	293	265	253	176	122	63	11
dsdp607B	780	730	703	n/a	586	510	488	454	408	361	311	259	206	184	128	91	11
md900963P	780	751	735	715	663	619	563	496	446	412	365	310	278	234	160	73	11
odp659B	780	723	702	673	664	595	558	519	456	389	345	285	237	189	123	73	11
odp663P	780	737	710	664	612	567	534	489	415	356	319	278	230	194	126	86	11
odp664B	780	728	693	660	599	564	527	480	411	368	321	288	228	177	118	82	11
odp677B	780	735	699	680	604	562	526	476	413	378	333	283	244	195	143	96	11
odp677P	780	723	702	676	603	555	527	470	412	368	330	287	243	191	142	99	11
odp758B	780	739	714	679	642	598	558	512	475	458	409	357	293	235	170	123	11
odp758P	780	746	725	691	649	602	562	508	477	450	404	341	290	236	170	128	11
odp806B	780	765	733	709	641	578	530	478	411	370	325	284	235	175	117	73	11
odp806P	780	756	730	705	635	572	528	485	419	367	334	276	232	174	115	72	11
odp846B	780	737	697	676	622	592	552	514	433	378	347	296	256	215	144	99	11
odp849B	780	751	721	712	642	596	558	518	450	404	372	314	276	228	136	82	11
odp851P	780	765	734	687	626	594	484	437	359	328	286	249	213	187	125	87	11
odp925B	780	735	715	698	633	581	553	515	424	379	329	306	231	191	119	75	11
odp927B	780	734	706	680	622	580	542	496	421	395	350	298	255	205	125	84	11
odp927P	780	732	704	688	619	582	542	496	423	386	342	293	248	203	125	84	11
odp980B	780	748	737	726	647	605	568	546	481	397	359	296	238	192	126	83	11
odp982B	780	750	723	684	611	576	529	453	366	286	245	210	170	132	95	78	11
odp982P	780	751	720	693	611	576	522	470	362	289	244	210	164	133	93	74	11
odp983B	780	738	721	686	621	562	504	449	396	328	289	244	198	151	102	80	11
v22-174P	780	736	707	679	612	565	490	433	400	375	346	305	269	224	158	106	11
v28-238P	780	741	718	684	654	615	561	530	481	415	375	305	266	213	133	86	11
v28-239P	780	738	712	672	605	541	506	465	393	363	329	287	236	196	123	78	11
Mean age	780	741	713	685	623	576	532	485	419	372	332	284	239	192	129	85	11
Uncertainty	3	5	7	8	9	10	11	11	11	11	10	10	9	8	7	6	1
SPECMAP	731	711	693	668	621	574	531	481	423	368	337	287	244	194	128	80	11
ODP677B	784	743	709	690	620	574	531	482	417	382	335	283	243	200	129	73	11
Devils Hole							519	461	416	383	340	287	251	195	142	81	
Vostok (GT-4)										383	327	277	240	202	133	85	15

[a]The events numbers are listed at top along with the parenthetical associated stage (Arabic) and termination (Roman) numbers. For comparison, the orbitally tuned SPECMAP stack [*Imbrie et al.*, 1984], orbitally tuned benthic ODP677 [*Shackleton et al.*, 1990], radiometric Devils Hole [*Winograd et al.*, 1997], and Vostok GT-4 deuterium age estimates [*Petit et al.*, 1999] are also shown.

[21] To estimate the uncertainty in ages due to accumulation rate variability, it is simplest to generate ensemble members from the stochastic accumulation model and calculate derived statistics from them. A synthetic accumulation rate with specified jitter (J) and power density (Φ) can be generated as

$$S(t) = \Im^{-1}\left\{\hat{\eta}\sqrt{J\Phi'(s, 1/40)}\right\} + 1, \qquad (12)$$

where $\Im^{-1}$ is the inverse Fourier transform, $\hat{\eta}$ is the Fourier transform of a white noise process, and $\Phi'(s, s_0) = \Phi(s, s_o)/\Sigma\Phi(s, s_0)$ where the sum is over all frequencies. Summing the accumulation rate gives a depth profile, $d(t) = \Sigma S(t)$, with the specified autocorrelation and jitter. By generating a large number of synthetic depth profiles and converting each to age with equation (7), a least squares best fit was sought between the observed and modeled $v_k^{(1)}$, $1 \leq k \leq 13$, distribution by varying the jitter in equation (12). A best fit was achieved with $J = 0.5$, and the resulting modeled $v^{(1)}$ and $v^{(2)}$ are shown in Figure 3. The autocorrelated random walk model reproduces the quadratic growth in $v^{(1)}$ and a single value of the jitter fits both the calculated $v^{(1)}$ and $v^{(2)}$ age variances. Further tests (not shown) indicate the autocorrelated random walk is equally consistent when greater numbers of age control points are used, and we will assume the same value of J is appropriate for our 17-ACP model. If s_o = 1/100 kyr, corresponding to the orbitally tuned accumulation estimates, the observations are fit equally well using a smaller value of J; with this method one cannot distinguish between the Devils Hole and orbital age model accumulation rate estimates in the marine cores.

4. Depth-Derived Age Model

[22] An age model based on a single linear age-depth relationship will be stretched or squeezed by every variation in sediment accumulation and each coring artifact. We seek to mitigate these age model errors by using multiple age-depth relationships. Table 2 indicates the $A_{j,k}^{(2)}$ event ages for each record along with the averages, $\overline{A}_k^{(2)}$. An age model based on these mean event ages, using

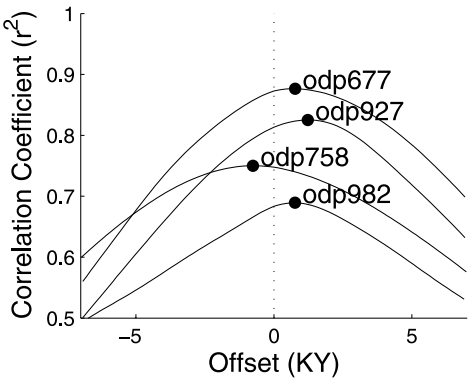

Figure 5. Lagged cross-correlation between sets of benthic and planktic $\delta^{18}O$ records measured in the same core. Positive values indicate a benthic lead.

all 17 events and termed the "depth-derived age model," may be expressed as

$$A_j^{(17)} = \frac{\bar{A}_k^{(2)} - \bar{A}_{k-1}^{(2)}}{d_{j,k} - d_{j,k-1}} d_j + \bar{A}_{k-1}^{(2)} \quad d_{j,k-1} \le d_j \le d_{j,k} \qquad 1 \le j \le 21 \qquad 2 \le k \le 17. \tag{13}$$

For each record, j, age is linearly interpolated with depth, d_j, between each pair of ACPs, $k-1$ and k, yielding a piecewise linear age model. $A_j^{(17)}$ is our best estimate of the core ages.

4.1. Uncertainty Analysis

[23] There are at least five sources of error in the $A^{(17)}$ age model: non-simultaneity between isotopic events, uncertainty in identifying the depth of each event, variations in accumulation rates, postdepositional processes, and uncertainty in the age of the B-M. Each source of error is considered in turn, and a Monte Carlo method is applied in conjunction with the stochastic sediment accumulation model to assess the overall uncertainty.

4.1.1. Simultaneity

[24] 1. The ocean mixing times for the $\delta^{18}O$ signal can range out to 1000 years and longer [*Wunsch*, 2003b]. Imposing simultaneity between $\delta^{18}O$ events, if correct, deblurs this mixing effect. To account for the ocean mixing time, a random variable with a ±1 kyr standard deviation is added to the $\delta^{18}O$ event ages in the stochastic sediment accumulation simulation.

[25] 2. This study incorporates benthic and planktic foraminiferal species over a wide geographic range. Foraminiferal $\delta^{18}O$ responds to both the temperature and $\delta^{18}O$ of their environments [e.g., *Schrag et al.*, 1996], and these environmental values likely fluctuate asynchronously and spatially heterogeneously. The presence of systematic offsets between benthic and planktic records can be estimated by means of a lagged cross-correlation when both species are measured in the same core. Figure 5 shows that the five benthic and planktic $\delta^{18}O$ pairs used here have a maximum cross-correlation at positions within a 1 kyr lag; a 1 kyr error is included in the stochastic accumulation model. More localized offsets between benthic and planktic records may occur in parts of the isotopic sequence, but we find no obvious pattern; if present, these localized offsets are apparently secondary to uncertainties associated with event identification.

4.1.2. Identification

[26] Owing to machine error in measuring $\delta^{18}O$, finite sampling resolution, and bioturbational blurring, events are only identifiable to within a finite depth range [*Pisias et al.*, 1984; *Huybers*, 2002]. For the mean accumulation rates of the cores sampled here, we estimate the depth uncertainty translates to approximately ±4 kyr. Larger errors are incurred if $\delta^{18}O$ events are misidentified, but we do not account for this possibility.

4.1.3. Accumulation Rate Variations

[27] 1. Core-site variations in accumulation rate will introduce errors in linear age-depth relationships, as discussed in section 3.3. Averaging multiple age-depth realizations, to the degree that they are independent, reduces this uncertainty. An empirical orthogonal functions (EOF, or "singular vector") analysis [e.g., *Wunsch*, 1996; *von Storch and Zwiers*, 1999] of accumulation rate variability, as estimated using $A^{(17)}$, indicates there are about 11 degrees of freedom in accumulation rate variations, and thus also in the age estimates.

[28] 2. Trends in global mean accumulation rates, as monitored at these 21 core sites, could bias the depth-derived age model. Spectra from both Devils Hole and from orbitally tuned chronologies, however, show low frequency white noise behavior (Figure 4) precluding long period global variations in accumulation. In agreement with this inference, *Lyle* [2003] found no evidence for spatially coherent long-period trends in Pacific carbonate accumulation during the Pleistocene. Thus, no uncertainties due to trends in accumulation are incorporated into the model.

[29] 3. Porosity is itself a climate variable and is known to change with other components of the climate system [*Herbert and Mayer*, 1991; *Hagelberg et al.*, 1995]. While random variations in porosity are implicitly accounted for in (2) above, climatically induced quasiperiodic age errors could contribute to the nonlinear and/or non-Gaussian structure of the $\delta^{18}O$ signal later discussed in section 5 [see also *Herbert*, 1994]. Changes in porosity are often linked with changes in organic and calcium carbonate deposition [*Herbert and Mayer*, 1991], and, it is likely that porosity-climate biases tend to cancel out when one aggregates cores from different ocean basins, owing to the opposite response of Pacific and Atlantic carbonate cycles. Furthermore, spectral estimates of sediment accumulation rate variations using the orbital age models (see Figure 4) show a smooth red noise trend both on a site-by-site basis and in the mean. This result indicates the absence of strong quasiperiodic variations in total accumulation rates, or alternatively that such variability is not resolved by orbital age estimates. In section 5.3 we further evaluate the potential influence of these quasiperiodic variations on our results.

4.1.4. Postdepositional Effects

[30] 1. Appendix A compares $A^{(17)}$ with a similar age model in which compaction is not accounted for. The latter

displays a bias with ages, on average, 10 kyr older than the compaction-corrected age model, but tapering to zero at the fixed end-points. Two sources of error exist in the compaction correction. First, scatter in the porosity measurements introduces uncertainty in determining the trend toward lower porosity with depth. Second, a larger source of uncertainty results from the absence of porosity measurements for 13 of the records, requiring an indirect compaction correction as discussed in Appendix A. The combined compaction correction uncertainty averages ±5 kyr. While large, this uncertainty is preferable to an age model bias which is expected to average 10 kyr. In future work, the decompaction uncertainty could be reduced by using more porosity measurements or, possibly, by accounting for differential compaction according to sediment composition.

[31] 2. The effects of coring on a sediment column are a further source of uncertainty for the depth-derived age model. Most of the records used here are from the advanced piston corer of the Ocean Drilling Program (ODP-APC) which uses a rigid drill pipe and a stationary piston in extracting cores. This drilling method reduces age-depth uncertainties related to over-sampling, a common problem for conventional non-rigid piston-corers, and uncertainties related to under-sampling, a common problem for gravity-corers [*Skinner and McCave*, 2003]. A remaining problem, however, is that the depth scale of cores obtained with the ODP-APC are typically stretched due to elastic rebound of the sediment after the core is recovered [*MacKillop et al.*, 1995; *Moran*, 1997]. The degree of rebound depends on sediment lithology and is likely to be heterogeneous. The high-frequency variations and down-core trends in age-depth relationships caused by sediment rebound are effectively folded into the previous estimates of accumulation rate variability and trends in sediment compaction. Because we seek only to estimate an age model, it is not necessary to disentangle these in situ and postcoring sources of uncertainty.

4.1.5. Brunhes-Matuyama Reversal

[32] *Singer and Pringle* [1996] estimate that the age of the B-M is radiometrically constrained to within ±2 kyr. However, the depth of the reversal however, is not always clearly identifiable [*Tauxe et al.*, 1996] and thus an additional uncertainty of ±4 kyr is added.

4.1.6. Monte Carlo Analysis

[33] The combined uncertainties associated with the depth-derived age model are incorporated into a stochastic age-depth model and estimated with a Monte Carlo analysis. All errors, except those associated with the compaction correction and accumulation rate variations, are modeled as independent realizations of a zero-mean Gaussian distribution. The expected squared error in the $\bar{A}_k^{(17)}$ age estimates is then

$$\langle e_k^2 \rangle = \frac{1}{21} 4^2 + 1^2 + 1^2 + 2^2 \big|_{k=17}, \quad 1 \le k \le 17. \tag{14}$$

The first term on the right is the event-depth determination error, assumed to be independent in each core and hence divided by the number of cores, 21. The second and third terms are the benthic/planktic timing error and the ocean signal propagation times. The last term is the estimated radiometric age error applied only for $k = 17$, the Brunhes-Matuyama. Apart from the depth determination error, each error is likely to be correlated between cores, and thus not effectively reduced by averaging.

[34] The compaction correction uncertainty, denoted c_k, is strongly correlated between events, biasing the entire age model toward either younger or older ages. Realizations of c_k are thus generated by multiplying the expected uncertainty structure (see Table 3) by a single value drawn from a zero-mean unit standard deviation Gaussian distribution.

[35] To account for the effects of jitter, a depth profile is generated according to equation (12) with $J = 0.5$ and $s_o = 1/40$ kyr. This depth profile nominally spans events 1 (10.6 kyr BP) to 17 (780 kyr BP), and has a true age, t, associated with each depth. Seventeen depths are identified such that

$$t(d_k) = \bar{A}_k \quad 1 \le k \le 17, \tag{15}$$

where each d_k represents the depth of a synthetic event and $\bar{A}_k$ are the fixed values estimated in equation (9). Applying equation (8), the depth profile is linearly converted to age yielding a jittered age estimate for each synthetic event. This process is repeated 11 times, corresponding to the approximately 11 degrees of freedom in accumulation rate estimates. Averaging over each of the synthetic records, j, yields a mean jittered age estimate,

$$\bar{A}'_k = \left(\frac{1}{11} \sum_{j=1}^{11} A'_{j,k} \right) + e_k + c_k, \quad 1 \le k \le 17, \tag{16}$$

to which the additional e_k and c_k error realizations are added. A prime is used to distinguish these synthetic realizations, $\bar{A}'_k$, from the real age estimates, $\bar{A}_k$.

[36] Applying equation (13) to equation (16) generates a single stochastic depth-derived age model realization. The root-mean square (rms) age deviation of numerous stochastic model realizations are used to estimate the expected $A^{(17)}$ age model uncertainty. Each event is a local minimum in uncertainty and events are spanned by short Brownian bridges. The event uncertainties are also tabulated in Table 2 and have a mean of ±9 kyr. As the magnitude of the short Brownian bridges is on the order of ±1 kyr and there are approximately 11 independent age-depth relationships, additional ACPs and independent age-depth relationships would only marginally reduce the uncertainty of this age model. Compared to the expected accuracy of most geochronological markers, particularly between the B-M and termination 2, the $A^{(17)}$ depth-derived age model has good age control.

[37] In section 5.1 the depth-derived age model is used in estimating the spectra of δ^{18}O records. It is expected that higher frequency processes will, in general, be more susceptible to age model jitter [*Moore and Thomson*, 1991; *McMillan et al.* 2002]. To gain a sense of jitter's influence on spectral estimates, consider the harmonic process

$$\mathcal{H}(t) = \cos(2\pi t/100) + \cos(2\pi t/41) + \cos(2\pi t/23). \tag{17}$$

Figure 6 shows successive periodograms of $H(t')$, where time, t, is stretched and squeezed to t' using an increasingly large jitter. Jitter is modeled as realizations of equation (16) with J increasing from zero to one and s_o = 1/40 kyr (see equation (11)). For comparison, periodograms of $H(t')$ are also shown with the jitter expected for a single age-depth relationship, i.e., equation (16) with $e_k = 0$ and without the summation. For a single age-depth relationship, the 100 kyr variability is poorly resolved, and the higher frequency variability is smeared into a red noise background. The depth-derived age model does considerably better at resolving the 100 kyr and 41 kyr (obliquity) variability, but nonetheless has significant spectral smearing associated with the 23 kyr variability. Thus, if present, excess precession band variability is expected to be poorly resolved.

4.2. Comparison With Other Age Models

[38] The $A^{(17)}$ age model makes no assumptions about orbital control of climate, and thus provides independent age estimates to compare against the orbitally tuned chronologies. Figure 7 shows the difference between $A^{(17)}$ and the orbitally derived age models for the SPECMAP stack [*Imbrie et al.*, 1984] and the ODP677 benthic δ^{18}O record [*Shackleton et al.*, 1990]. The SPECMAP orbital age estimates beyond 625 kyr BP are generally considered too young, due to an incorrect B-M age [e.g., *Shackleton et al.*, 1990; *Singer and Pringle*, 1996], and ages beyond termination 7 for SPECMAP are adopted from the orbitally tuned ODP677 chronology. There are up to 2 kyr differences between termination ages listed in *Imbrie et al.* [1984] and in Table 2 due to our use of the δ^{18}O midpoint in defining termination depths; also note there are typographical errors for the termination 5 and 7 ages in the *Imbrie et al.* [1984] table. Using the Table 2 ages, the root-mean square (rms) event age discrepancies between the depth and orbital age models are 3 kyr (SPECMAP) and 5 kyr (ODP677). Considering $A^{(17)}$ has an estimated uncertainty of ±9 kyr and SPECMAP one of ±5 kyr, the depth-derived chronology is consistent with the orbitally derived age estimates.

[39] The depth-derived age estimate for termination 2 closely agrees with the orbitally derived age estimates (128 kyr BP), thus supporting the younger termination 2 radiometric age estimates [e.g., *Broecker et al.*, 1968; *Bard et al.*, 1990] over the older ages [e.g., *Gallup et al.*, 2002; *Henderson and Slowey*, 2000]. Note, however, this conclusion is directly dependent upon the compaction correction which shifts the mean termination 2 age from 139 to 129 kyr BP (see Table 3; at termination 2 uncertainties in the compaction correction are about ±4 kyr.) Using a depth-tuning approach, but not correcting for compaction, *Raymo* [1997] estimated an age of 136 kyr BP for termination 2 and concluded this age was anomalously old due to sediment extension in the upper core. In general, however, the magnitude of sediment extension is expected to increase down-core because of the greater changes in effective stress [*Moran*, 1997; *MacKillop et al.*, 1995]. Acting alone, greater extension with depth would give anomalously young ages. The anomalously old ages are more readily explained by a down-core increase in compaction which, because compaction is partially plastic [*Moran*, 1997], is not fully compensated for by postcoring sediment rebound. If uncorrected, this residual trend in compaction leads to the anomalously old termination 2 ages (see Table 3).

[40] Figure 7 also compares the Vostok deuterium (δD) ages (*Petit et al.* [1999], GT-4 ice age) with the $\bar{A}^{(17)}$ event ages. Clearly, the δD of Antarctic ice (Vostok) and δ^{18}O need not have a simple relationship with marine foraminiferal δ^{18}O records. Nonetheless, the RMS age deviation between GT-4 and $\bar{A}^{(17)}$ is only 6 kyr (events 1 through 8 only), and is within the expected uncertainty of the depth-derived age model. More striking in Figure 7 is the tendency of some of the Devils Hole event dates to differ markedly from those of the deep-sea cores, beyond the one-sigma error estimates of both data types. Devils Hole has an RMS age deviation with $\bar{A}^{(17)}$ (events 2 through 11) of 11 kyr where the depth-derived chronology is relatively younger between terminations 2 and 5, and older beyond termination 5. One should not infer from this result that either is incorrect: as noted, there is no necessity in the climate system for open ocean changes to be contemporaneous with those nearshore or over continents [*Winograd et al.*, 1997].

[41] Of the available Pleistocene age models, $\bar{A}^{(17)}$ most closely accords with the orbitally tuned age estimates. Because the orbital and depth-derived age models were estimated using completely independent assumptions, their approximate accord encourages the belief that there is real skill in both of them. Nonetheless, as we will see, the differences between them have important consequences for the interpretation of the climate record.

5. The δ^{18}O Signal and Nonlinear Climate Change

[42] We now turn our attention away from the age models and toward the δ^{18}O signal itself. To extract a well resolved and representative signal from the ensemble of 26 δ^{18}O records, the leading empirical orthogonal function (EOF1) is calculated from the five planktic and five benthic records with an accumulation rate of 3 cm/kyr or greater and the smallest available mean sampling interval (see Table 1). EOF1 explains 78% of the δ^{18}O variance and represents an almost uniformly weighted average of the ten best resolved δ^{18}O records, thus making it similar to a mean or "stacked" record. For comparison, the leading EOFs of the five best resolved benthic records (EOFb) and planktic records (EOFp) are also calculated (see Figure 8). EOFb and EOFp are very similar to EOF1: each has a squared cross-correlation with EOF1 of 0.97. The squared cross-correlation between EOFp and EOFb is 0.89, indicating the ubiquity of the oceanic δ^{18}O signal. Given these high correlations, it is not surprising that the spectral description of EOF1 presented in the following sections also holds for EOFb and EOFp.

[43] Figure 8 shows EOF1 from $A^{(17)}$ and the SPECMAP δ^{18}O stack [*Imbrie et al.*, 1984] on its orbitally tuned age model. The SPECMAP age model was constructed by imposing a constant phase relationship between the obliquity and precessional orbital parameters and the respective frequency bands in five separate δ^{18}O records [*Imbrie et al.*,

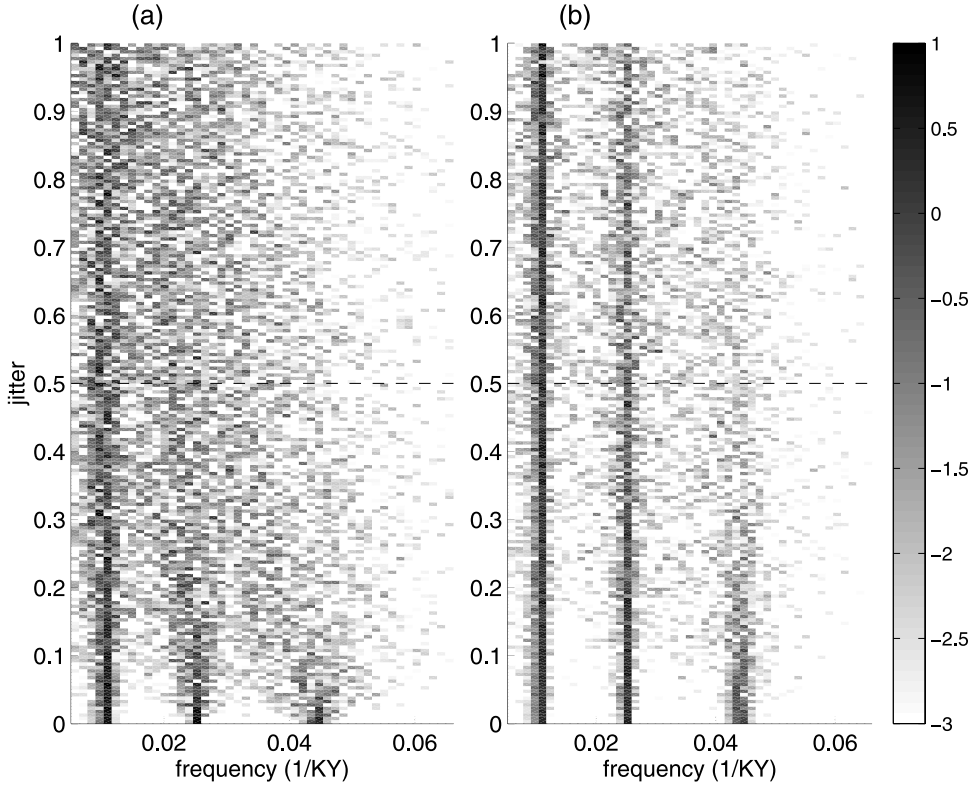

Figure 6. The impact of age model jitter on the power spectrum of a harmonic process, $\mathcal{H}$ (equation (17)). Shading indicates the logarithm of the power estimate plotted against frequency (1/kyr) and the degree of jitter where s_o = 1/40 kyr (see equation (11)). Both plots show spectra of $\mathcal{H}$ after distorting its timescale according to the specified jitter: (a) has errors as expected for a single age-depth relationship, while (b) has errors as expected for the depth-derived age model. The degree of jitter expected in a real core is 0.5, and is indicated by the horizontal dashed line. In Figure 6a, only the 100 kyr band can be distinguished, while Figure 6b retains good resolution of the 100 and 41 kyr bands and a semblance of the 23 kyr band.

1984]. The five orbitally tuned δ^{18}O records were then averaged to form the stack. The initial discussion here compares EOF1 with the SPECMAP stack; afterward, for purposes of comparison, an orbitally tuned version of EOF1 is also investigated.

[44] The ten δ^{18}O records used in EOF1 are independent of the five SPECMAP stack records, yet the isotopic variations in the SPECMAP stack and EOF1 are strongly similar in timing, number, and amplitude. That there is only a 3 kyr RMS age model difference between the SPECMAP stack and EOF1 is rather remarkable. When pinned to their respective independent age models, the squared correlation between EOF1 and SPECMAP is 0.68. This is a higher correlation than between the exclusively planktic SPECMAP stack and EOFp, even when the single high-latitude planktic record from ODP982 is excluded from EOFp.

5.1. Spectral Description of the δ^{18}O Record

[45] The spectral distribution of the SPECMAP stack, shown in Figure 9, has a power law relationship with frequency, s^{-q}, $q \approx 2.7$ and spectral peaks lying above the approximate 95% level-of-no-significance in the 1/100, 1/41 (obliquity), 1/23 and 1/18 kyr (precession) bands relative to the background continuum. Bands are defined as the interval ±1/400 kyr about the central frequency. The SPECMAP distribution of energy has been widely accepted as accurately representing long-period δ^{18}O variability [e.g., *Imbrie et al.*, 1993] with the spectral peaks in the obliquity and precession bands commonly interpreted as showing linear responses to the respective orbital variations [e.g., *Hagelberg et al.*, 1991]. Of course, this obliquity and precession prominence is assumed in the orbital tuning. Note in particular that the energy fraction lying in the obliquity and precessional bands is a small fraction of the record total. The origins of the 100 kyr band variability are much more contentious owing to the paucity of insolation forcing in this band. Climatic resonance, nonlinear climatic response, and additional forcing mechanisms have all been postulated as explanations for the 100 kyr-band variability (for a review, see *Elkibbi and Rial* [2001]). *Roe and Allen* [1999] point out the difficulty in differentiating among these competing 100 kyr-band orbital theories, and there is some doubt whether an orbital relationship exists at all [*Wunsch*, 2003a].

[46] The depth-derived age model provides a somewhat different perspective on δ^{18}O variability. The periodogram

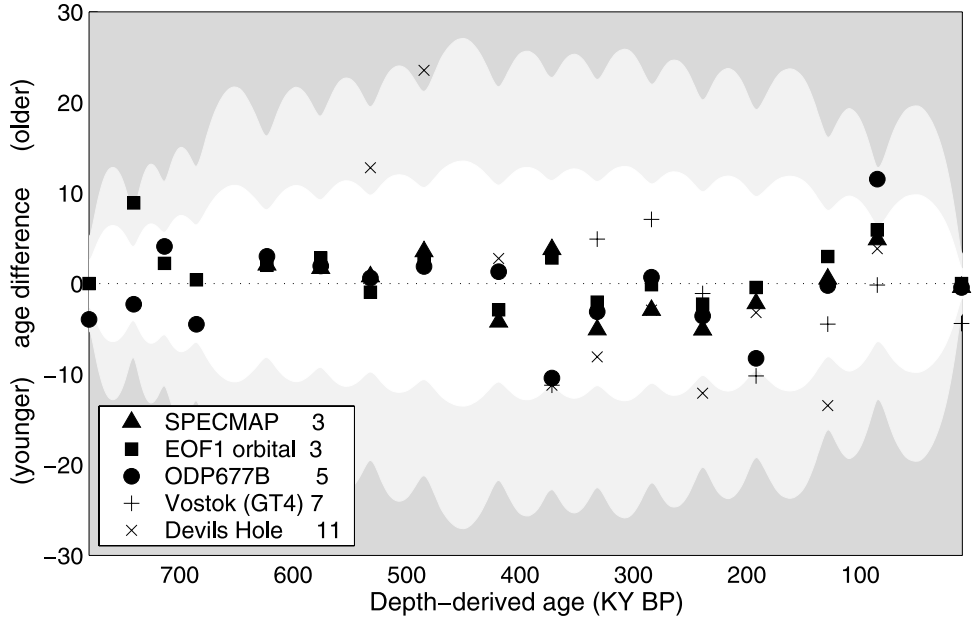

Figure 7. The $A^{(17)}$ depth-derived age model relative to other $\delta^{18}O$ age models. Negative values indicate the depth-derived age model is relatively younger. Root mean square age model differences are listed in the legend. Depth-derived ages are most consistent with the orbitally derived age estimates. The inner and outer gray clouds respectively indicate the one and two standard deviation depth-derived age model uncertainty. Within two standard deviations, all age models are consistent with the depth-derived ages.

of EOF1, shown in Figure 9, has a power law, like that of the SPECMAP stack, with $q \approx 2.7$. But unlike the SPECMAP result six, rather than four, spectral bands are above the approximate 95% level-of-no-significance at 1/100, 1/70, 1/41, 1/29, 1/23, and 1/18 kyr. A simple relationship between the central frequencies, $s(n)$, of these bands is

$$s(n) = \frac{1}{41} + \frac{n}{100}, \quad -1 \leq n \leq 3. \tag{18}$$

$s(n)$ is written in terms of the 1/41 kyr band (obliquity) rather than the 1/23 or 1/18 bands (precession) because the 1/41 kyr band accounts for a greater fraction of the $\delta^{18}O$ variability.

[47] The energy in the 1/100, 1/41 ($n = 0$), 1/23 and 1/18 kyr ($n = 2, 3$) bands has been much discussed. Excess energy near 1/70 and 1/29 kyr has also been noted in the literature [e.g., *Nobes et al.*, 1991; *Yiou et al.*, 1991; *Bolton and Maasch*, 1995; *Mix et al.*, 1995b]. The simple rule embodied in equation (18) is strongly suggestive of a spectral structure resulting from a weak nonlinear interaction of the obliquity band with the 100 kyr band. The conventional interpretation, referred to as the "pacemaker" hypothesis [*Hays et al.*, 1976], requires that the timing of the very energetic quasi-100 kyr variability be controlled by the weaker high frequency elements. Here it appears that the most energetic bands (100 kyr, 41 kyr) interact to produce sum and difference frequencies, as is typical of a weakly nonlinear system. A complication of the conclusion is the possibility that the enhanced precession band energy is due, all or in part, to overtones of the obliquity band response.

5.2. Higher-Order Spectral Analysis

[48] A higher-order statistic, the autobicoherence, aids in distinguishing the behaviors of EOF1 and the SPECMAP stack age model. The 95% level-of-no-significance for autobicoherence, computed by Monte Carlo methods for Gaussian red noise with a power law of minus two, is 0.7 along the diagonal ($s_1 = s_2$) and 0.55 off the diagonal ($s_1 \neq s_2$). Appendix D discusses the autobicoherence test in more detail. Before examining autobicoherence in the $\delta^{18}O$ records, the nature of the possible forcing is investigated using a test signal,

$$T(t) = \theta(t) + p(t), \tag{19}$$

where θ is obliquity and p is precession as calculated by *Berger and Loutre* [1992]. Both components of $T(t)$ are normalized to have unit standard deviation and zero mean. Because the origins of the 100 kyr band are so uncertain, no corresponding forcing term is included. The completely deterministic $T(t)$ displays a number of significant autobicoherencies (see Figure 10) related to the amplitude and frequency modulations inherent to these orbital parameters [e.g., *Hinnov*, 2000]. The strong autobicoherence at (1/41, 1/41) highlights the potentially ambiguous origins of the precession band; that is, the first harmonic of obliquity (2/41 kyr) and the precession band (1/23 to 1/18) overlap. Note that a rectification of the annual cycle is required for

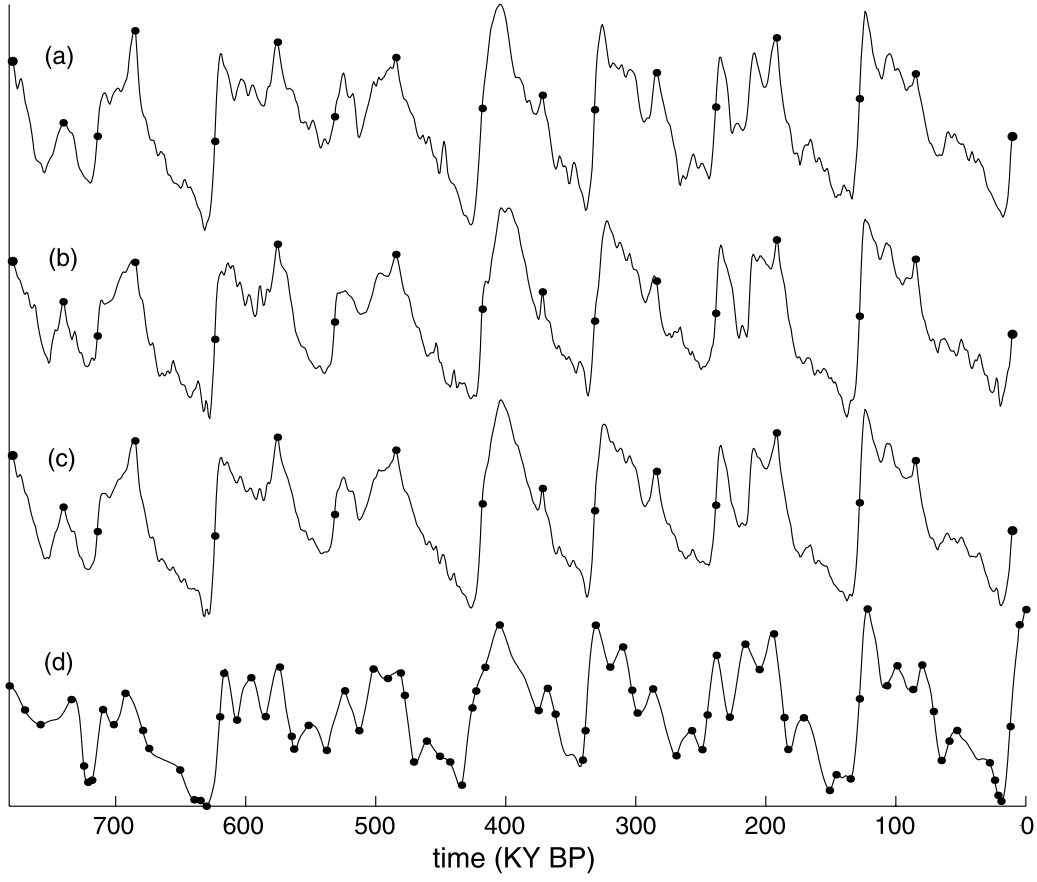

Figure 8. (a) The leading empirical orthogonal function of the five best resolved planktic records (EOFp) and (b) the five best resolved benthic records (EOFb). The squared cross-correlation between EOFb and EOFp is 0.89. (c) The leading EOF of both the best resolved benthic and planktic records (EOF1). Each EOF is on the depth-derived age model. (d) The SPECMAP stack on its orbitally tuned age model. The squared cross-correlation between the SPECMAP stack and EOF1 is 0.68, slightly higher than the correlation between SPECMAP and either EOFb or EOFp. Dots indicate the location of ACPs used for the depth-derived and SPECMAP stack age models.

long-term precessional variability to appear in a record [*Rubincam*, 1994; *Huybers and Wunsch*, 2003], and that such rectification is also expected to generate harmonics of the obliquity energy.

[49] Significant autobicoherence can indicate the presence of a nonlinearity in a record, or that the distribution is non-Gaussian, or both (nonlinear records are usually non-Gaussian). Here $T(t)$ is non-Gaussian (it is deterministic). The distribution of the δ^{18}O record, shown as a histogram of δ^{18}O measurements from the 26 records shown in Table 1, appears in Figure 10. The δ^{18}O signal has a skewness of -0.1 and a kurtosis of 2.5, clearly indicating its non-Gaussian nature and as with $T(t)$, interpretation of the autobicoherence must account for this fact.

[50] The autobicoherences of EOF1 and the SPECMAP stack are shown in Figure 11. The SPECMAP estimate displays significant autobicoherence at frequency pairs (1/70, 1/70), (1/70, 1/41), and (1/41, 1/29), a pattern which resembles that of $T(t)$, on which the chronology of SPECMAP is based. The SPECMAP autobicoherencies which are most emphasized however, involve the 1/70 and 1/29 kyr bands, and unlike EOF1, these bands display no significant concentrations of energy. *Hagelberg et al.* [1991] also find evidence of a (1/80, 1/41) autobicoherence in the orbitally tuned ODP 677 benthic and planktic δ^{18}O records, which given the coarseness of their frequency resolution, is indistinguishable from the SPECMAP (1/70, 1/41) pair.

[51] EOF1 displays a gridded pattern of autobicoherencies: all combinations of frequencies in equation (18) with integers $-1 \leq n \leq 2$ are coincident with significant local maxima in autobicoherence except for (1/29, 1/29) and (1/23, 1/23). Whether the autobicoherence arises from non-Gaussian statistics in the forcing, or nonlinearity in the response, its distinct frequency structure supports the inference of weak interband interaction within the climate system. The absence of bicoherence at the strongest precession band (1/23, 1/23) points to obliquity's central role in this coupling.

5.3. Importance of Age Models

[52] There are important differences between EOF1 and the SPECMAP δ^{18}O stack: SPECMAP has more than three

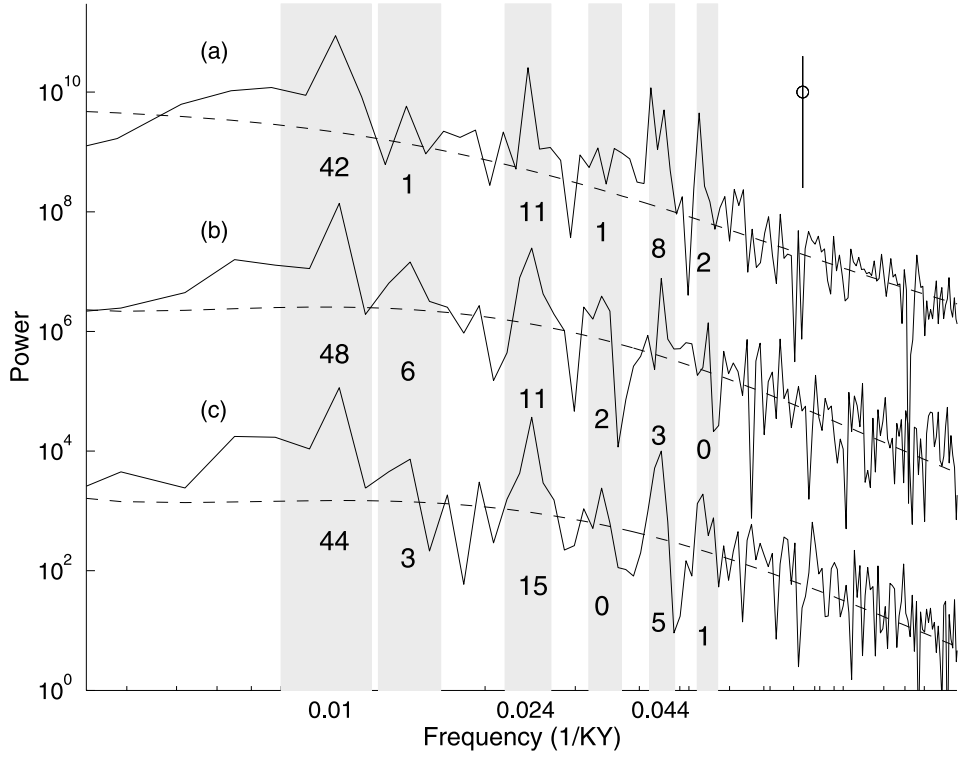

Figure 9. Periodograms are (a) SPECMAP, (b) EOF1, and (c) the orbitally tuned EOF1. For presentation purposes, each periodogram, after the first, is shifted downward by two orders of magnitude. Dashed lines are third-order polynomials fit to the noise background of each periodogram. Numbers are the percentage of energy contained within each band (1/100, 1/70, 1/41, 1/29, 1/23, and 1/18 kyr) above the background noise level; the 1/100 kyr band accounts for almost half of the total energy within each spectrum. The approximate 95% confidence interval (from χ^2 with two degrees of freedom) is indicated by the vertical bar in the upper right hand corner; the open circle represents the expected background level.

times the energy concentrated within the precession band but no discernible concentration of energy at 1/70 and 1/27 kyr; furthermore the autobicoherent features are significantly different. The small amount of precession band energy in EOF1 may be a result of age model jitter (see Figure 6). We attribute the remaining differences to the orbital tuning of the SPECMAP age model; support for this hypothesis is provided by considering the effects of jittering SPECMAP and orbitally tuning EOF1.

[53] Monte Carlo simulations indicate that random age model errors tend to diminish both concentrations of spectral energy and autobicoherence, making such errors an unlikely explanation for the structure in EOF1. Quasiperiodic age model errors, however, can create spurious structure in spectral estimates (see section 4.1; *Herbert* [1994]). To examine this possibility, the spectral and autobicoherence structures of SPECMAP were examined after distorting the age model using periodic and quasiperiodic functions. The most relevant results occur for 100 kyr periodic distortions of the SPECMAP age model, yielding significant concentrations of energy at the 1/70 and 1/27 kyr bands. Similarly, distorting SPECMAP ages in proportion to the δ^{18}O signal yields a concentration of energy at 1/70 kyr. All of these age model errors, however, tend to decrease

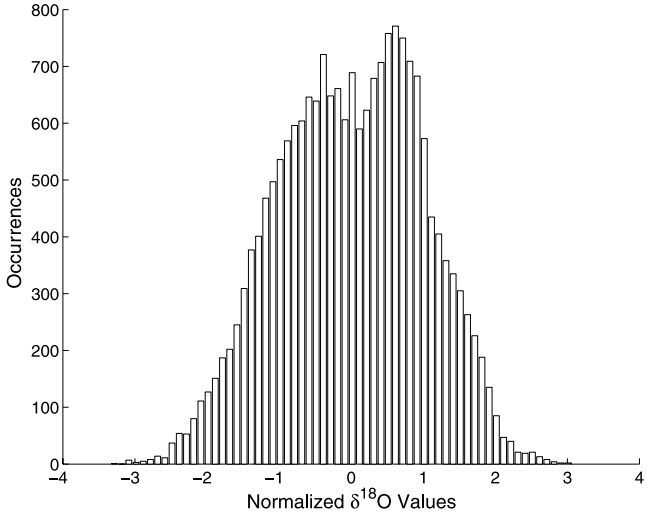

Figure 10. Histogram of δ^{18}O measurements between 10 to 780 kyr BP from the 26 records listed in Table 1.

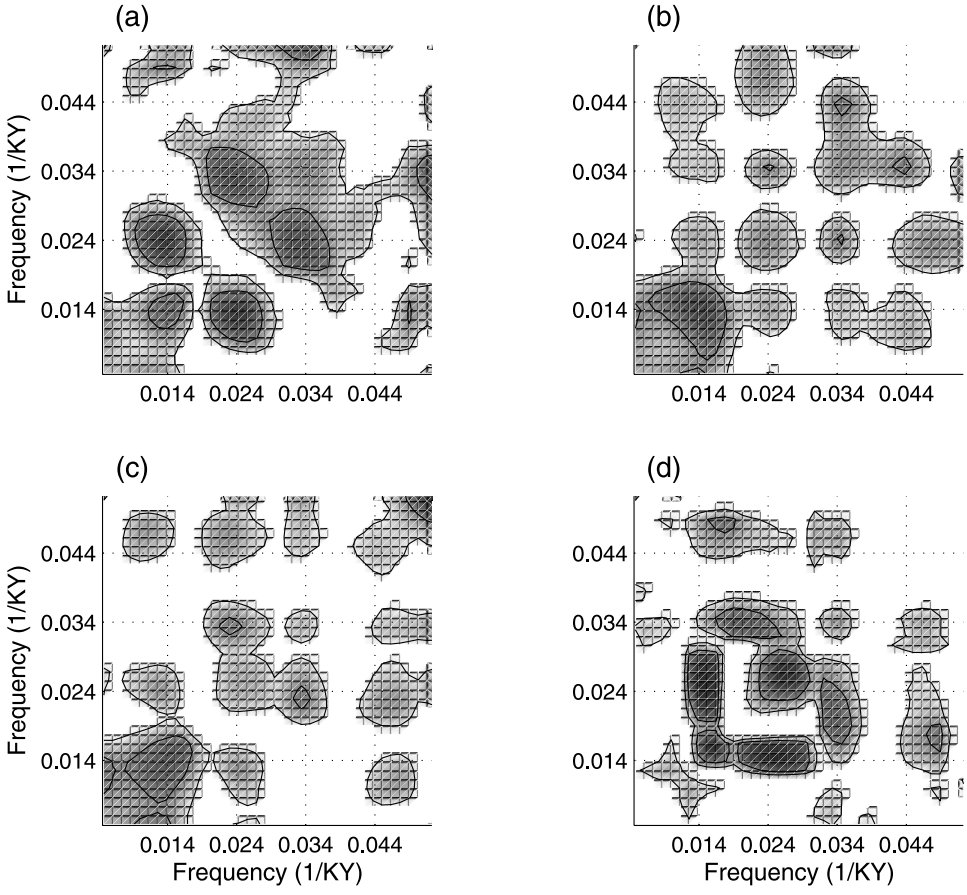

Figure 11. Autobicoherence of (a) SPECMAP, (b) EOF1, (c) orbitally tuned EOF1, and (d) the orbital test signal, $T(t)$. The tick marks on the frequency axes are given by equation (18). Contour intervals are at 0.5 and 0.7; respectively, the 95% level of no significance for off-diagonal and diagonal features.

autobicoherence without making the pattern appear more like that of EOF1.

[54] On the other hand, in Appendix C, we show that the orbital tuning of EOF1 makes its spectra and autobicoherence pattern appear more similar to the SPECMAP stack. It is further demonstrated, using synthetic signals, that orbital tuning tends to suppress evidence of weak nonlinearity in a record, by shifting energy out of overtone and interaction bands and into the Milankovitch bands. We thus conclude that orbital tuning tends to suppress evidence of real nonlinearity in the $\delta^{18}O$ record.

6. Conclusions

[55] Age models assigned to paleoclimatic records strongly influence the inferences drawn about past climate behavior. Variations in sediment accumulation rate cause errors in linear age-depth models, so that a simple linear age-depth relationship is often not sufficiently accurate to yield meaningful results. Use of orbital tuning to remove these age model errors, however, suppresses evidence of nonlinearity at low frequencies in the system.

[56] An alternative to orbital tuning is to estimate sediment core age using spatial mean sediment accumulation rates, and in conjunction with an important compaction correction, this alternative is used at 21 core sites to construct a depth-derived age model spanning the last 780 kyr. The observed error in linear age-depth relationships is modeled as an autocorrelated stochastic process, and the $A^{(17)}$ age model is estimated to be accurate to within ±9 kyr. The depth-derived ages make no assumptions regarding orbital control, but agree with the orbitally tuned age models to within ±5 kyr, and thus within the error limits are consistent with one another. The remaining discrepancies, however, have important consequences.

[57] Spectral analysis of EOF1, using the $A^{(17)}$ age model, indicates significant spectral energy at combination tones of the 1/100 kyr and obliquity bands. There is also significant autobicoherence between each of these bands in EOF1, all of which indicates a weakly nonlinear climatic response to obliquity forcing interacting with the quasi-100 kyr variability. These results may aid in differentiating between the various mechanisms proposed to explain glacial interglacial climate variability.

Appendix A: Compaction Correction

[58] Sediment compaction is, to first order, a function of pressure and lithology [e.g., *Athy*, 1930; *Baldwind and Butler*, 1985]; factors such as time, temperature, and pore

water chemistry are generally secondary. Because pressure increases with depth, systematic down-core compaction is expected, and this phenomenon is observed in a wide variety of marine cores [e.g., *Baldwind and Butler*, 1985; *Bahr et al.*, 2001]. Postcoring sediment rebound partially compensates for in situ compaction, but because compaction is more plastic at higher pressure [e.g., *Moran*, 1997], residual down-core trends toward greater compaction are retained. Variations in lithology can also modify the compaction profile, for instance clay deposited above limestone can lead to reduced compaction with depth [e.g., *Schwarzacher*, 1975], but there is no reason to expect such structures to be systematically present in the global array of cores studied here. Climatically driven quasiperiodic changes in compaction are addressed in sections 4.1 and 5.3.

[59] The effect of compaction on linear age-depth relationships is discussed qualitatively by *Hays et al.* [1976], *Williams et al.* [1988], and *Raymo* [1997]. Here a quantitative age correction function is developed for gross trends in compaction and then applied to the depth scale of each core. *Athy* [1930] first showed an increasing load on porous sediment results in pore water draining from the sediment matrix and an exponentially decreasing porosity. Porosity, ϕ, is the fraction of sediment volume occupied by water,

$$\phi = 1 - \frac{\rho}{\rho_d}, \tag{A1}$$

where ρ is the bulk density, and ρ_d is the dry density.

[60] Given a functional relationship between depth and porosity, it is possible to estimate the effects of compaction on a linear age model. Take $h = 0$ and $t = 0$ as the sediment height and date of the B-M magnetic reversal. Sediment accumulates at a rate S so that

$$h = \int_0^t S(t)dt, \tag{A2}$$

and without compaction, the final height would be, $H = \overline{S}T$. $\overline{S}$ is the mean accumulation rate, H and T are the final-time values of h and t.

[61] If compaction is assumed to result solely in the upward expulsion of pore water [e.g., *Berner*, 1990], the compacted and un-compacted sediment column heights are related by

$$h = \int_0^{h'} \frac{1-\phi'}{1-\phi} dh', \tag{A3}$$

where primes indicate the compacted quantity. For the moment, assume postdepositional compaction is present, but accumulation rates are constant. Then, if age is taken to be linear with depth between $h = 0$ and $h = H$, an error is incurred as

$$\delta t = t' - t = T\left(\frac{h}{H} - \frac{h'}{H'}\right). \tag{A4}$$

The age error is zero at the top, $h = H$, $h' = H'$, and bottom, $h = h' = 0$, but between these fixed points errors occur to the degree that h' is a nonlinear function of time. If compaction increases with depth, as expected, a layer of sediment between the top and bottom has $h/H > h'/H'$, $\delta t > 0$, and compacted age estimates which are erroneously old.

[62] To illustrate the possible effects of compaction on an age model, assume that ϕ is constant and that compaction occurs at a linear rate with depth, c, such that $\phi' = \phi - c(H' - h')$. Inserting this porosity relationship into equation (A3) and integrating yields

$$h = h' + \frac{ch'}{(1-\phi)}\left(H' - \frac{h'}{2}\right). \tag{A5}$$

Substituting equation (A5) into equation (A4) and writing $h' = Ht'/T'$ gives

$$\delta t = t'\left(\frac{1 - \phi + cH'(1 - t'/(2T))}{1 - \phi + cH'/2} - 1\right). \tag{A6}$$

Plausible values for equation (A6) are $\phi = 0.7$, $c = .001$ m/m, $H' = 30$ m, and $T = 800$ kyr, yielding a maximum age offset, $\delta t = 9$ kyr at 400 kyr BP. Equation (A6) shows that offsets toward older ages will increase with greater porosity, compaction, and accumulation rate.

[63] Figure 12 shows the porosity profile plotted against depth for eight ODP cores located in the eastern equatorial Pacific (ODP846, 849, and 851; Leg 138 ODP Initial Reports CD-ROM), Ceara Rise (ODP925 and 927; Leg 154 Log and Core Data CD-ROM, Borehole Research Group, LDO), and the N. Atlantic regions (ODP980, 982, and 983; Leg 162 Log and Core Data CD-ROM, Borehole Research Group, LDO) measured using gravimetric techniques [*Boyce*, 1976]. The eastern equatorial Pacific group shows a general trend of decreasing porosity with depth superimposed on a large degree of scatter where the scatter is in-part attributable to variations in lithology, coring effects, and measurement error.

[64] For the eight cores in which data are available, porosity trends are estimated from 400 m below the seafloor to the core top. For the eastern equatorial Pacific cores, a line is fit to each porosity profile, and for the Ceara Rise and North Atlantic cores a second-order exponential is used. ODP980 was alone in showing no discernible trend. Assuming that the estimated trends in porosity reflect inhomogeneities in relative compaction, we apply a compaction correction based on conservation of dry sediment volume [e.g., *Berner*, 1990],

$$h(1-\phi) = h'(1-\phi'). \tag{A7}$$

Here the thickness of a compacted sediment layer, h', is adjusted to thickness, h, by adjusting the down-core trend in porosity, $\phi'(h')$, to a constant value, ϕ. Note, the depth-derived ages are insensitive to the choice of reference porosity, ϕ, because they are pinned to a constant age at termination 1 and the B-M.

Table 3. Decompacted Age Corrections in Kiloyears Applied to Each Core Where All Age Corrections Produce a Relatively Younger Age Model[a]

	Event (Associated Stage/Termination)																
	17 (19.1)	16 (18.3)	15 (VIII)	14 (17.1)	13 (VII)	12 (15.1)	11 (VI)	10 (13.11)	9 (V)	8 (11.1)	7 (IV)	6 (8.5)	5 (III)	4 (7.1)	3 (II)	2 (5.1)	1 (I)
dsdp502P	0	2	4	5	8	9	10	11	12	12	12	11	10	8	6	3	0
dsdp552B	0	2	4	5	8	10	10	11	12	12	11	11	11	9	7	4	0
dsdp607B	0	3	5	7	11	14	15	16	17	17	17	17	15	14	11	8	0
md900963P	0	2	3	5	8	11	13	16	17	18	19	19	18	17	14	8	0
odp659B	0	3	4	6	6	9	11	12	13	14	15	14	13	12	9	5	0
odp663P	0	3	5	7	10	12	14	15	17	17	17	17	16	15	11	8	0
odp664B	0	3	6	7	11	12	14	15	16	17	17	17	15	13	10	7	0
odp677B	0	3	5	6	10	12	14	15	17	17	17	17	16	14	12	9	0
odp677P	0	4	5	7	10	13	14	15	17	17	17	17	16	14	12	9	0
odp758B	0	2	3	4	6	7	8	9	10	10	10	11	10	9	8	6	0
odp758P	0	2	2	4	5	7	8	9	10	10	10	10	10	9	8	6	0
odp806B	0	1	2	4	7	9	10	11	12	13	13	12	11	10	7	5	0
odp806P	0	1	3	4	7	9	10	11	12	12	12	12	11	9	7	4	0
odp846B	0	2	3	3	5	5	6	7	7	7	7	7	7	6	4	3	0
odp849B	0	0	1	1	1	2	2	2	2	2	2	2	2	2	1	1	0
odp851P	0	0	1	2	3	3	4	4	4	4	4	4	3	3	2	2	0
odp925B	0	5	7	9	15	20	22	24	29	30	30	30	28	26	20	13	0
odp927B	0	5	7	10	14	17	20	22	25	26	27	27	26	24	18	14	0
odp927P	0	5	7	9	15	17	20	22	26	26	27	27	26	24	18	14	0
odp980B	0	3	4	5	12	15	17	19	22	25	25	25	24	22	17	12	0
odp982B	0	2	3	5	8	9	10	12	13	12	12	11	10	8	6	5	0
odp982P	0	1	3	4	7	9	10	11	13	12	12	11	10	8	6	5	0
odp983B	0	5	6	10	16	21	25	28	30	31	31	30	28	24	19	15	0
v22-174P	0	2	3	5	7	8	10	11	11	11	11	11	11	10	8	6	0
v28-238P	0	2	3	4	5	6	8	9	10	10	11	10	10	9	6	4	0
v28-239P	0	1	2	3	5	6	6	7	7	7	7	7	6	6	4	2	0
mean	0	3	4	5	8	10	12	13	15	15	15	15	14	13	10	7	0
σ	0	1	2	2	3	4	4	5	5	6	6	6	5	5	4	3	0

[a]Event numbers are listed at top along with parenthetical associated stage (Arabic) and termination (Roman) numbers. At bottom are the mean correction and the associated uncertainty. The applied corrections are a continuous function of depth, but are listed only at the 17 selected events.

[65] Although it is highly likely that trends in compaction exists at all, or most, of the core sites [e.g., *Bahr et al.*, 2001], the compaction correction has considerable uncertainty for the thirteen sites at which porosity measurements are not available. Standard decompaction formula are only applicable at depths well below that of the B-M [*Baldwind and Butler*, 1985; *Bahr et al.*, 2001] (greater than 200 m), and we choose to use the mean of the seven identified porosity trends (see Figure 12) as the basis for decompacting the remaining fourteen cores according to equation (A7), to include ODP980. To estimate the associated uncertainty, each of the fourteen cores are also decompacted using the individual porosity-depth trends, yielding seven estimates of decompacted depth. Age is then estimated from each realization of the decompacted depth scale according to equation (13), and the standard deviation of these ages is taken as the estimated uncertainty.

[66] Table 3 lists the age correction resulting from decompaction at each event for each $\delta^{18}O$ record and the uncertainty in the mean age off-set. All corrections make the $\delta^{18}O$ events relatively younger and range from zero at the endpoints to 15 kyr at 350 kyr BP. While uncertainties range up to 6 kyr, they are always less than half the magnitude of the estimated bias, and thus decompaction is inferred to significantly improve the accuracy of the depth-derived age estimates.

Appendix B: XCM Tuning Algorithm

[67] A simple and repeatable algorithm, termed XCM (cross-correlation maximizer), is used for objective tuning. In common with most such methods [e.g., *Martinson et al.*, 1982; *Bruggerman*, 1992; *Lisiecki and Lisiecki*, 2002], the algorithm adjusts the timescale of a record, $\psi(t')$, in relation to a target record, $\tau(t)$, while seeking to maximize a given quantity; in this case, the squared cross-correlation coefficient,

$$r^2 = \left(\frac{\sum_t \psi(t' + \mu(t'))\tau(t)}{\sqrt{\sum_t \psi(t' + \mu(t'))^2}\sqrt{\sum_t \tau(t)^2}} \right)^2 . \qquad \text{(B1)}$$

Here $\mu(t')$ is the time adjustment function. For the applications presented in this paper, $\tau(t')$ and $\psi(t')$ are discretely sampled at 1-kyr intervals and age control points (ACPs) are assigned to $\psi(t')$ at specified intervals. A simulated annealing optimization method [*Press et al.*, 1999] is then applied to estimate the arrangement of ACPs

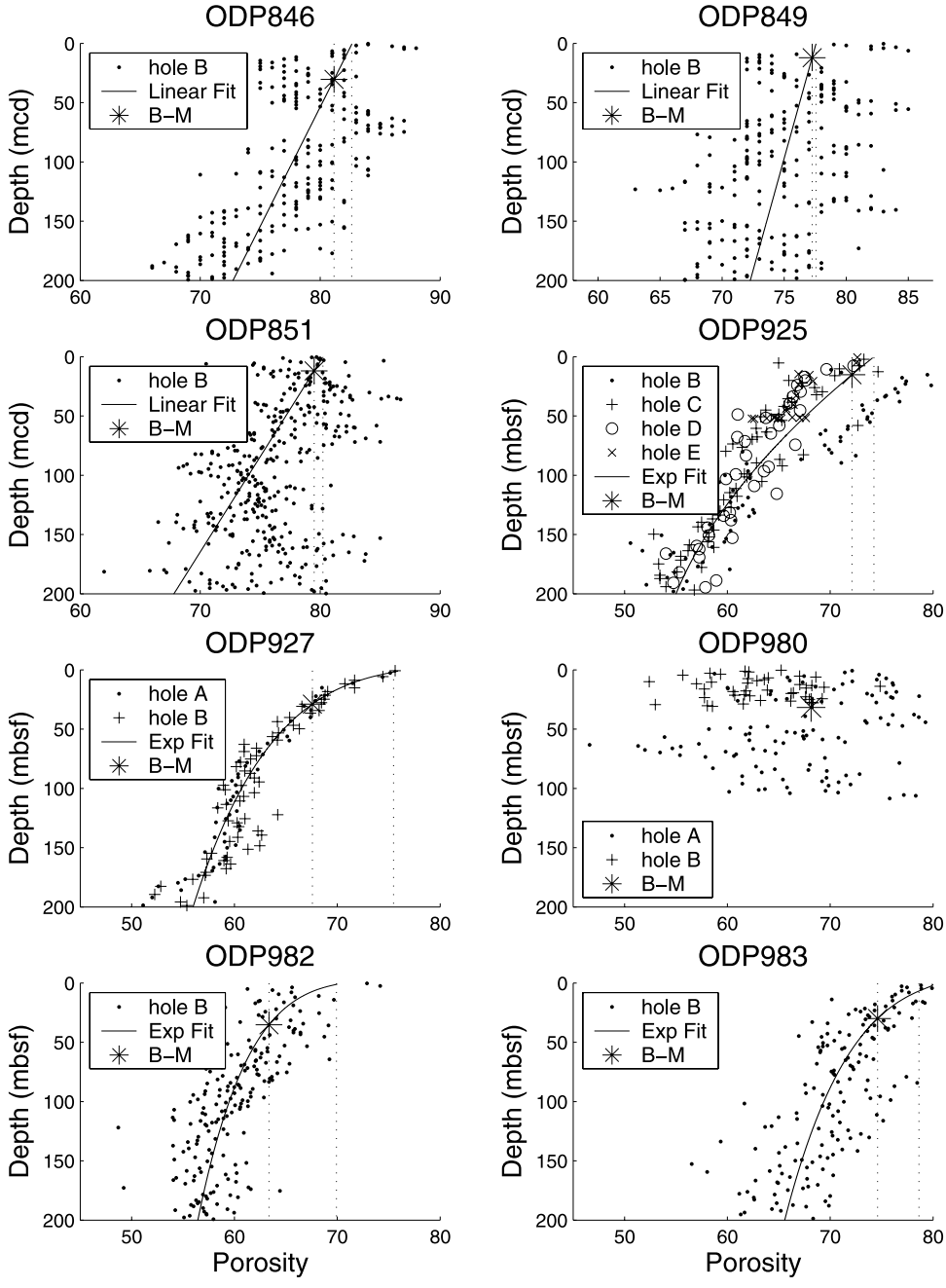

Figure 12. Changing porosity with depth in ODP cores from the eastern equatorial Pacific, Ceara Rise, and North Atlantic. An exponential curve or straight line (whichever is better) was fit to each porosity profile, except for ODP980, which showed no distinct pattern. The vertical dotted lines bound the change in porosity between termination 1 and the B-M.

which maximizes the cross-correlation. To prevent unrealistic changes in implied accumulation rates, XCM may be constrained to not stretch or squeeze time beyond a specified factor. The final control-point arrangement provides a piecewise linear approximation to $\mu(t')$. It should be noted that XCM may significantly increase the cross-correlation between two records without there being any true relationship (see Appendix C).

[68] Most tuning algorithms employ narrow band-pass filtering to isolate the Milankovitch band of interest. A difficulty with this approach is that even slight errors in the preliminary age model can smear spectral energy across the entire frequency range [e.g., *Martinson et al.*, 1987]. This mistiming results in a form of aliasing of the spectral power, and like all aliasing, no filter can undo it. Thus we have chosen not to filter records prior to tuning, and instead use

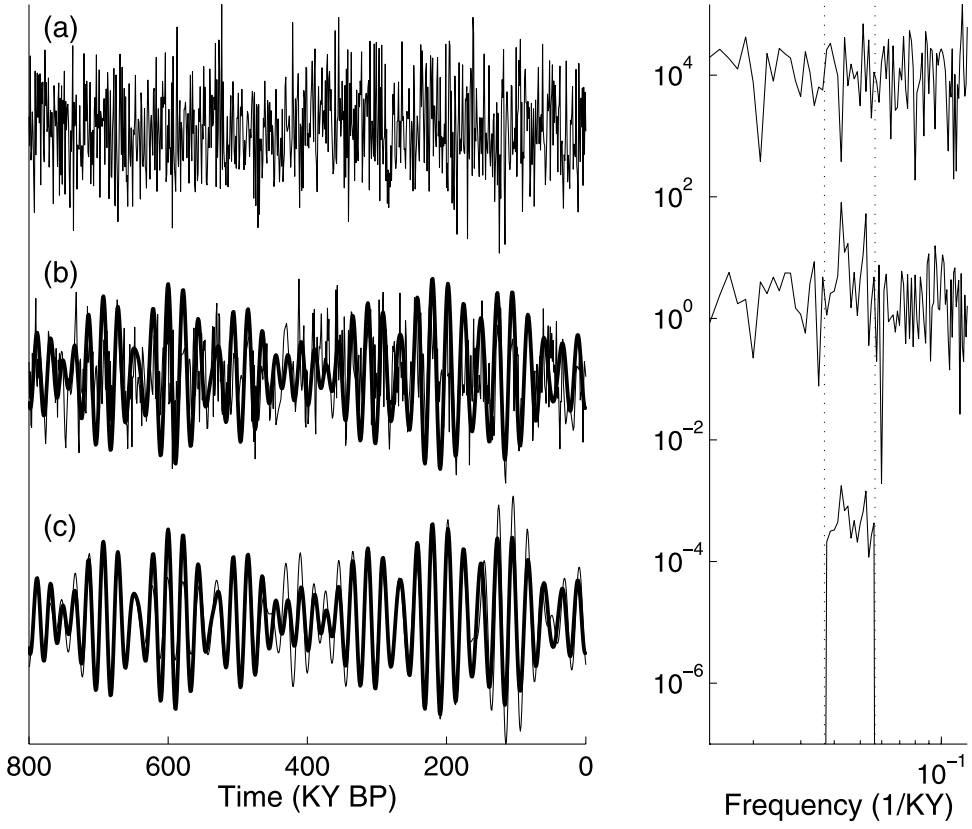

Figure 13. Results from the orbital tuning of white noise. (a) Time series of white noise. (b) Precession curve (thick line) and same white noise process tuned to precession (thin line). (c) Band-pass filtered, tuned white noise (thin line), and the precession curve. Note that the band-pass filtered white noise shows an amplitude modulation similar to the precession curve. Right panel displays the power density spectra of the original white noise (top), of the tuned white noise (middle), and of the band-pass filtered tuned white noise (bottom). These spectra are displaced in the vertical by a factor of 10^4 for visual clarity, and the vertical dotted lines delineate the precession band, 1/23 to 1/18 kyr.

what is termed the direct response approach [*Martinson et al.*, 1987].

Appendix C: Impact of Orbital Tuning

[69] If climate linearly responds to insolation variations, one would expect the modulation structure of the forcing to be at least qualitatively mimicked in the response. If one seeks to tune to precession, this assumption is immediately complicated by the requirement for a rectifier to be present [*Rubincam*, 1994; *Huybers and Wunsch*, 2003]. Nonetheless, assuming some climatic response to insolation forcing, a multitude of methods have been used to orbitally tune paleoclimatic records. The criteria generally used to assess the accuracy of an orbitally tuned timescale [e.g., *Imbrie et al.*, 1984; *Bruggerman*, 1992; *Shackleton et al.*, 1995] are that geochronological data should be respected within their estimated accuracies, sedimentation rates remain plausible, variance should become concentrated at the Milankovitch frequencies with a high coherency between the orbital signal and the data, and (what is often referred to as the clinching argument) similar amplitude modulation should appear in the Milankovitch derived insolation functions and in the orbitally tuned result.

[70] To comply with the criteria for a successful orbital tuning result, the XCM algorithm is constrained to not stretch or squeeze a record by more than a factor of four, thus keeping accumulation rates within plausible levels. Considering the difficulty of determining geochronological dates in the interval between termination two (approximately 130 kyr BP) and the Brunhes-Matuyama (B-M) boundary (approximately 780 kyr BP), it seems unlikely the available geochronological constraints would conflict with most tuning results. Three signals are selected to demonstrate the impact of orbital tuning: EOF1, white noise, and a weakly nonlinear signal.

C1. EOF1

[71] The selected target curve for orbitally tuning EOF1 is

$$\tau(t) = \sqrt{.2}\theta'(t) + \sqrt{.8}p'(t). \tag{C1}$$

The primes indicate the phases of obliquity and precession are each phase-lagged assuming a linear response with a time constant of 17 kyr, consistent with the orbital target curves of *Imbrie et al.* [1984]. Rather than iteratively tuning to precession and obliquity respectively, as done by the

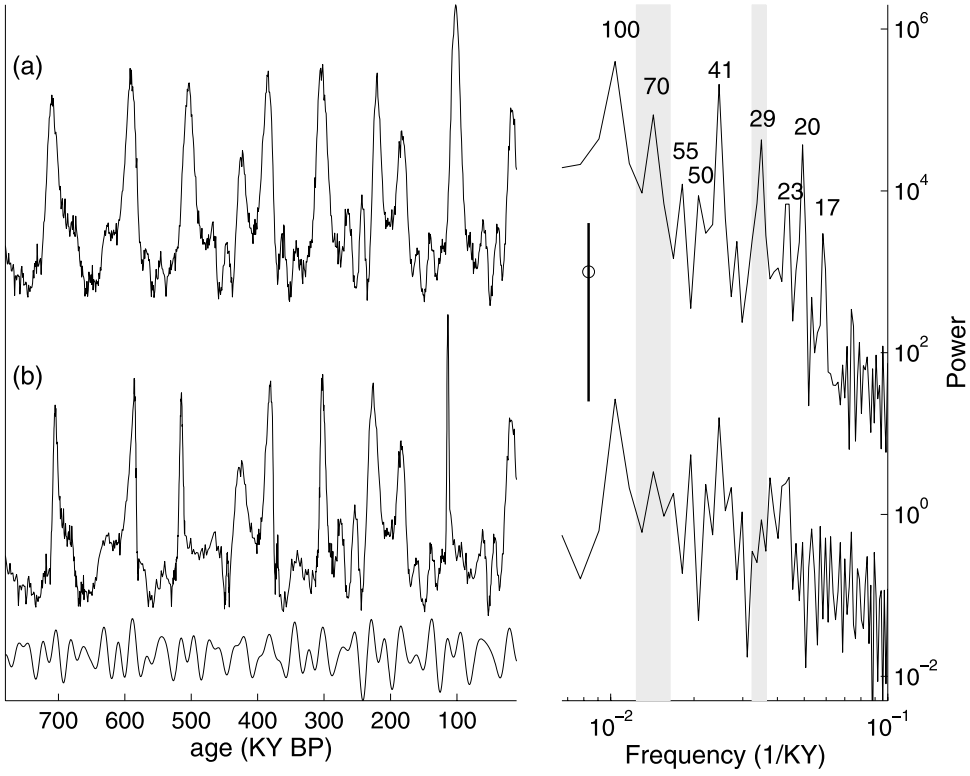

Figure 14. (a) The orbital signal $\psi(t)$ from equation (C2) (left) and its associated periodogram (right). The linear components of $\psi(t)$ give spectral peaks at 1/100; 1/55, a sideband of obliquity; and 1/41 kyr, the main obliquity band. The nonlinear components give spectral peaks at 1/70, the 1/100 − 1/41 combination tone; 1/50, the 2/100 overtone; 1/29, the 1/100 + 1/41 combination tone; 1/23, an interaction tone; 1/21, the 2/41 overtone; and 1/17 kyr, another interaction tone. (b) After a small degree of orbital tuning, assuming a linear response to obliquity and precession (bottom curve), the signal is visually similar but the periodogram has concentrations of energy primarily at the 100 kyr, obliquity, and precession bands. The approximate 95% confidence interval for red noise is indicated by the vertical bar.

SPECMAP group, the two parameters are combined into a single target curve, $\tau(t)$, with precession accounting for 80% of the total variance. ACPs are assigned to the $A^{(17)}$ age model every eight kyr, and XCM was used to maximize the cross-correlation between EOF1 and $\tau(t)$.

[72] The difference between the $A^{(17)}$ and the fully orbitally tuned EOF1 age model is shown in Figure 7. Not surprisingly, orbital tuning brings $A^{(17)}$ into close agreement with the SPECMAP and orbital ODP677 age models. The periodogram (Figure 9c) and autobicoher-

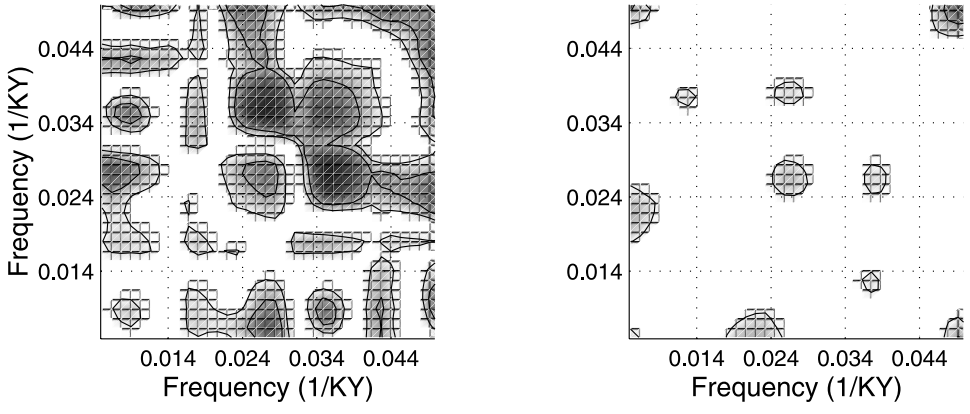

Figure 15. The autobicoherence of $\psi(t)$ before (left) and after (right) orbital tuning. Significant autobicoherence is indicated by light shading for the off-diagonal and dark shading for the on-diagonal.

ence (Figure 11c) of the orbitally tuned EOF1 now resemble those from SPECMAP. In particular, orbital tuning enhances the obliquity and precession peaks in EOF1 while diminishing the 1/29 and 1/70 kyr spectral peaks and making the (1/70, 1/29) and (1/41, 1/41 kyr) autobicoherence appear insignificant. The spectrum of EOF1 is sensitive to the process of orbital tuning, and assuming a linear response to obliquity and precession imposes a behavior consistent with the SPECMAP analysis.

C2. Noise

[73] It is also useful to investigate signals with known statistical properties. We begin with a white noise Gaussian distributed process, $\psi(t')$, and tune it to the precession parameter [*Berger and Loutre*, 1992] over a 800 kyr period. A typical realization of XCM tuning is presented in Figure 13 where the squared cross-correlation is increased from zero to 0.19. Consistent with the results of *Neeman* [1993], a concentration of variance at the triplet of precessional peaks occurs, coherence in the precession band is greater than 0.9 (0.65 is the approximate 95% level-of-no-significance), and both amplitude and frequency modulation similar to the precession parameter appears, completely spuriously. When band-pass filtered, the imposed frequency modulations produce amplitude modulations in the tuned signal [see *Huybers*, 2002]. Similar results hold when red noise, rather than white noise, is orbitally tuned. Thus precession-like amplitude modulation in an orbitally tuned record does not guarantee the accuracy of an age model.

C3. Nonlinear Signal

[74] Finally, the observations regarding EOF1 in section 5 motivate investigation of another signal,

$$\psi(t) = 2\cos(2\pi t/100) + \theta(t) + 0.5(\cos(2\pi t/100) + \theta(t))^2, \quad \text{(C2)}$$

involving linear and nonlinear contributions from a 100 kyr harmonic and zero-mean unit variance obliquity variability. The relative amplitudes are selected to reflect the distribution of variance observed in EOF1, and for statistical stability, a small amount of white noise is added. As evident from the periodogram in Figure 14, the nonlinearity generates variability at a number of combination and over-tones. A potentially confusing result is that energy appears at the first overtone of the main obliquity band 1/21 kyr, and, because of the frequency and amplitude modulation inherent to obliquity, at interaction bands of 1/23 and 1/17 kyr. Without knowing the form of $\psi(t)$, a triplet of spectral peaks at these frequencies could readily be mistaken for evidence of precession variability.

[75] Figure 14 also shows $\psi(t')$ after orbital tuning to the target curve, $\tau(t)$, given in equation (C1). Typical results increase the squared cross-correlation between the target curve and ψ from 0.1 to 0.25. After tuning, the nonlinear spectral peaks are suppressed while precession period variability is enhanced. Similarly, Figure 15 shows that the autobicoherent structure of $\psi(t)$ is almost totally obscured by the orbital tuning, all of which indicates that orbital tuning will suppress evidence of real nonlinearity.

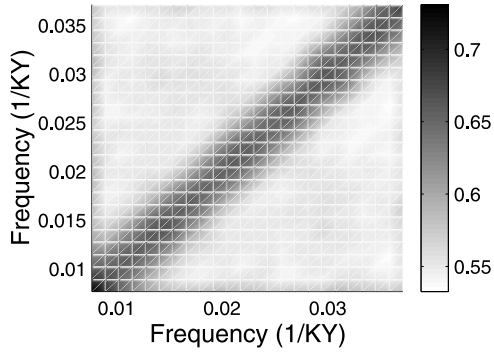

Figure 16. Results of a Monte Carlo estimate indicating the approximate level below which 95% of autobicoherence estimates, made using Gaussian red noise, are expected to occur by chance. The results are symmetric about the diagonal, and values are roughly 0.55 for $k \neq l$ and 0.7 for $k = l$.

Appendix D: Autobicoherence

[76] A test for quadratic coupling was presented by *Hasselmann et al.* [1963] and used to evaluate weak nonlinearities in shallow water wave propagation. When two harmonics are coupled so as to modulate one another, a third harmonic with a particular frequency and phase is expected,

$$S(t) = e^{2\pi i f_k t + \phi_k} e^{2\pi i f_l t + \phi_l} = e^{2\pi i (f_k + f_l) t + \phi_k + \phi_l}.$$

[77] To test for this relationship, we define the bispectrum as

$$B_{k,l} = \langle \hat{S}_k \hat{S}_l \hat{S}^*_{k+l} \rangle,$$

where $\hat{S}_k$ is the discrete Fourier transform of $S(t)$ at frequency k, S^* is the conjugate ($S^*_{k+l} = S_{-k-l}$), and $\langle\rangle$ indicates the expected value. Unless $\phi_{k+l} = -(\phi_k + \phi_l)$, $B(k, l)$ will be complex. The magnitude of $B(k, l)$ depends on both the magnitude of the complex Fourier coefficients, $|\hat{S}_k||\hat{S}_l||\hat{S}_{k+l}|$, and the stability of the phase relationship between the coefficients i.e., for random phasing $\langle \hat{S}_k \hat{S}_l \hat{S}_{k+l} \rangle = 0$. The autobicoherence is defined as

$$C_{k,l} = \frac{\langle \hat{S}_k \hat{S}_l \hat{S}_{k+l} \rangle}{\langle |\hat{S}_k||\hat{S}_l||\hat{S}_{k+l}| \rangle},$$

where the denominator represents $B(k, l)$ for the case of perfect phase coherence, and $0 \leq C_{k,l} \leq 1$. The expected value of the autobicoherence is estimated here by adapting the bispectral routine presented by *Muller and MacDonald*

[2000]. The algorithm consists of subtracting the mean value of $S(t)$, applying a Hanning window, and estimating the autobicoherence as

$$C_{k,l} = \frac{\left|\sum_{k-2}^{k+2}\sum_{l-2}^{l+2} a_{k,l}\hat{S}_k\hat{S}_l\hat{S}_{k+l}\right|}{\sum_{k-2}^{k+2}\sum_{l-2}^{l+2} a_{k,l}\left|\hat{S}_k\right|\left|\hat{S}_l\right|\left|\hat{S}_{k+l}\right|},$$

$$a_{k+n,l+m} = \frac{1}{\sqrt{(k-n)^2+(l-m)^2}},\ n,m \in \{-2,-1,1,2\},\ a_{k,l} = 1,$$

where $a_{k,l}$ is a weighting coefficient. A Monte Carlo method was used to estimate uncertainty levels for autobicoherence computed according to the above algorithm. Figure 16 shows the approximate 95% level-of-no-significance to reject the null hypothesis of Gaussian distributed red noise; levels are roughly 0.55 for $k \neq l$ and 0.7 for $k = l$. A significant autobicoherence can also indicate the presence of a non-Gaussian signal, thus care is required in interpreting the result.

[78] **Acknowledgments.** This work benefited from comments by O. Aharonson, M. Bender, E. Boyle, W. Curry, T. Herbert, J. Landwehr, L. Lisiecki, J. McManus, D. McMillan, D. Oppo, M. Raymo, I. Winograd, and two anonymous reviewers; W. Curry also pointed out the importance of sediment compaction to age-depth relationships. Funding was provided by the National Defense Science and Engineering Graduate Fellowship Program.

References

Athy, L. (1930), Density, porosity and compaction of sedimentary rocks, *AAPG Bull.*, *14*, 1–24.

Bahr, D., J. Hutton, E. Syvitski, and L. Pratson (2001), Exponential approximations to compacted sediment porosity profiles, *Comput. Geosci.*, *27*, 691–700.

Baldwind, B., and C. Butler (1985), Compaction curves, *Am. Assoc. Petrol. Geol. Bull.*, *69*, 622–626.

Bard, E., B. Hamelin, and R. Fairbanks (1990), U-Th ages obtained by mass spectrometry in corals from Barbados: Sea level during the past 130,000 years, *Nature*, *346*, 241–244.

Bassinot, F., E. Beaufort, L. Vincent, F. Labeyrie, P. Rostek, Muller, X. Quidelleur, and Y. Lancelot (1994), Coarse fraction fluctuations in pelagic carbonate sediments from the Tropical Indian Ocean: A 1500-kyr record of carbonate dissolution, *Paleoceanography*, *9*, 579–599.

Berger, A., and M. F. Loutre (1992), Astronomical solutions for paleoclimate studies over the last 3 million years, *Earth Planet. Sci. Lett.*, *111*, 369–382.

Berger, W., M. Yasuda, T. Bickert, G. Wefer, and T. Takayama (1994), Quaternary timescale for the ontong java plateau: Milankovitch template for Ocean Drilling Program site 806, *Geology*, *22*, 463–467.

Berner, R. (1990), *Early Diagenesis*, Princeton Univ. Press, Princeton, N. J.

Bhattacharya, R. N., and E. C. Waymire (1990), *Stochastic Processes With Applications*, John Wiley, Hoboken, N. J.

Bickert, T., W. Curry, and G. Wefer (1997), Late Pliocene to Holocene (2.6–0 MA) western equatorial Atlantic deep water circulation: Inferences from benthic stable isotopes, *Proc. Ocean Drill. Program Sci. Results*, *154*, 239–253.

Bolton, E., and K. Maasch (1995), A wavelet analysis of Plio-Pleistocene climate indicators: A new view of periodicity evolution, *Geophys. Res. Lett.*, *22*, 2753–2756.

Boyce, R. (1976), Definitions and laboratory techniques of compressional sound velocity parameters and water-wet content, wet-bulk density, and porosity parameters by gravimetric and gamma ray attenuation techniques, *Initial Rep. Deep Sea Drill. Proj.*, *33*, 931–958.

Broecker, W. (1984), Terminations, in *Milankovitch and Climate, Part 2*, edited by A. Berger et al., pp. 687–698, D. Reidel, Norwell, Mass.

Broecker, W., D. Thurber, J. Goddard, T. Ku, R. Matthews, and K. Mesolella (1968), Milankovitch hypothesis supported by precise dating of coral reefs and deep-sea sediments, *Science*, *159*, 297–300.

Bruggerman, W. (1992), A minimal cost function method for optimizing the age-depth relationship of deep-sea sediment cores, *Paleoceanography*, *7*, 467–487.

Channell, J., D. Hodell, and B. Lehman (1997), Relative geomagnetic paleointensity and $\delta^{18}O$ at ODP site 983, *Earth Planet. Sci. Lett.*, *153*, 103–118.

Chen, J., J. Farrell, D. Murray, and W. Prell (1995), Timescale and paleoceanographic implications of a 3.6 m.y. oxygen isotope record from the northeast Indian Ocean (Ocean Drilling Program Site 758), *Paleoceanography*, *10*, 21–47.

Cullen, J., and W. Curry (1997), Variations in planktonic foraminifer faunas and carbonate preservation at site 927: Evidence for changing surface water conditions in the western tropical Atlantic Ocean during the middle Pleistocene, *Proc. Ocean Drill. Program Sci. Results*, *154*, 207–228.

Curry, W., and J. Cullen (1997), Carbonate production and dissolution in the western equatorial Atlantic during the last 1 MY, *Proc. Ocean Drill. Program Sci. Results*, *154*, 189–199.

de Menocal, P., W. Ruddiman, and E. Pokras (1993), Influences of high- and low-latitude processes on african terrestrial climate: Pleistocene eolian records from equatorial Atlantic Ocean Drilling Program site 663, *Paleoceanography*, *8*, 209–242.

Elkibbi, M., and J. Rial (2001), An outsider's review of the astronomical theory of the climate: Is the eccentricity-driven insolation the main driver of the ice ages?, *Earth Sci. Rev.*, *56*, 161–177.

Feller, W. (1966), *An Introduction to Probability Theory and Its Applications*, John Wiley, Hoboken, N. J.

Flower, B. (1999), Planktonic foraminifers from the Subpolar North Atlantic and Nordic Seas: Sites 980–987 and 907, *Proc. Ocean Drill. Program*, *162*, 19–34.

Gallup, C. D., H. Cheng, F. W. Taylor, and R. L. Edwards (2002), Direct determination of the timing of sea level change during Termination II, *Science*, *295*, 310–314.

Hagelberg, T., N. Pisias, and S. Elgar (1991), Linear and nonlinear couplings between orbital forcing and the marine $\delta^{18}O$ record, *Paleoceanography*, *6*, 729–746.

Hagelberg, T., N. Pisias, L. Mayer, N. Shackleton, and A. Mix (1995), Spatial and temporal variability of Late Neogene equatorial Pacific carbonate: Leg 138, *Proc. Ocean Drill. Program Sci. Results*, *138*, 321–336.

Hasselmann, K., W. Munk, and G. MacDonald (1963), Bispectra of ocean waves, in *Proceedings of the Symposium on Time Series Analysis*, edited by M. Rosenblatt, pp. 125–139, John Wiley, Hoboken, N. J.

Hays, J., J. Imbrie, and N. Shackleton (1976), Variations in the Earth's orbit: Pacemaker of the ice ages, *Science*, *194*, 1121–1132.

Henderson, G., and N. Slowey (2000), Evidence from U-Th dating against Northern Hemisphere forcing of the penultimate deglaciation, *Nature*, *404*, 61–66.

Herbert, T. (1994), Readings orbital signals distorted by sedimentation: Models and examples, in *Orbital Forcing and Cyclic Sequences*, edited by P. de Boer and D. Smith, pp. 483–507, Blackwell Sci., Norwell, Mass.

Herbert, T., and L. Mayer (1991), Long climatic time series from sediment physical property measurements, *J. Sediment. Petrol.*, *61*, 1089–1108.

Herbert, T., J. Schuffert, D. Andreasen, L. Heusser, M. Lyle, A. Mix, A. Ravelo, L. Stott, and J. Herguera (2001), Collapse of the California current during glacial maximum linked to climate change on land, *Science*, *293*, 71–76.

Hinnov, L. (2000), New perspectives on orbitally forced stratigraphy, *Annu. Rev. Earth Planet. Sci.*, *28*, 419–475.

Huybers, P. (2002), Depth and orbital tuning: A new chronology of glaciation and nonlinear orbital climate change, MS thesis, Mass. Inst. of Technol., Cambridge, Mass.

Huybers, P., and C. Wunsch (2003), Rectification and precession signals in the climate system, *Geophys. Res. Lett.*, *30*(19), 2011, doi:10.1029/2003GL017875.

Imbrie, J., J. Hays, D. Martinson, A. McIntyre, A. Mix, J. Morley, N. Pisias, W. Prell, N.

Shackleton (1984), The orbital theory of Pleistocene climate: Support from a revised chronology of the marine delta 18 O record, in *Milankovitch and Climate, Part 1*, edited by A. Berger et al., pp. 269–305, D. Reidel, Norwell, Mass.

Imbrie, J., et al. (1993), On the structure and origin of major glaciation cycles: 2. The 100,000-year cycle, *Paleoceanography*, *8*, 699–735.

Johnson, R. (1982), Brunhes-Matuyama magnetic reversal dated at 790,000 yr BP by marine-astronomical correlations, *Quat. Res.*, *17*, 135–147.

Karner, D., and F. Marra (1998), Correlation of fluviodeltaic aggradational sections with glacial climate history: A revision of the Pleistocene stratigraphy of Rome, *Geol. Soc. Am. Bull.*, *110*, 748–758.

Karner, D., and R. Muller (2000), A causality problem for Milankovitch, *Science*, *288*, 2143–2144.

Lisiecki, L. E., and P. A. Lisiecki (2002), Application of dynamic programming to the correlation of paleoclimate records, *Paleoceanography*, *17*(D4), 1049, doi:10.1029/2001PA000733.

Lyle, M. (2003), Neogene carbonate burial in the Pacific Ocean, *Paleoceanography*, *18*(3), 1059, doi:10.1029/2002PA000777.

MacKillop, A., K. Moran, K. Jarret, J. Farrell, and D. Murray (1995), Consolidation properties of equatorial Pacific Ocean sediments and there relationship to stress history and offsets in the leg 138 composite depth sections, *Proc. Ocean Drill. Program Sci. Results*, *138*, 357–369.

Martinson, D. G., W. Menke, and A. Stoffa (1982), An inverse approach to signal correlation, *J. Geophys. Res.*, *87*, 4807–4818.

Martinson, D. G., N. G. Pisias, J. D. Hays, J. Imbrie, T. C. Moore, and N. J. Shackleton (1987), Age dating and the orbital theory of the ice ages—Development of a high-resolution 0- to 300,000-year chronostratigraphy, *Quat. Res.*, *27*, 1–29.

McManus, J., D. Oppo, and J. Cullen (1999), A 0.5 million year record of millennial-scale climate variability in the North Atlantic, *Science*, *283*, 971–975.

McManus, J., D. Oppo, L. Keigwin, J. Cullen, and G. Bond (2002), Thermohaline circulation and prolonged interglacial warmth in the North Atlantic, *Quat. Rev.*, *58*, 17–21.

McManus, J., D. Oppo, J. Cullen, and S. Healey (2003), Marine isotope stage 11 (MIS 11), Analog for Holocene and future climate?, in *Earth's Climate and Orbital Eccentricity: The Marine Isotope Stage 11 Question*, vol. 137, edited by A. Droxler et al., pp. 69–85, AGU, Washington, D. C.

McMillan, D., C. Constable, and R. Parker (2002), Limitations on stratigraphic analyses due to incomplete age control and their relevance to sedimentary paleomagnetism, *Earth Planet. Sci. Lett.*, *201*, 509–523.

Milankovitch, M. (1941), *Kanon der Erdbestrahlung und seine Andwendung auf das Eiszeitenproblem*, R. Serb. Acad., Belgrade.

Mix, A., N. Pisias, W. Rugh, J. Wilson, A. Morey, and T. Hagelberg (1995a), Benthic foraminifer stable isotope record from site 849 (0–5 ma): Local and global climate changes, *Proc. Ocean Drill. Program Sci. Results*, *138*, 371–412.

Mix, A., J. Le, and N. Shackleton (1995b), Benthic foraminifer stable isotope stratigraphy of site 846: 0–1.8 ma, *Proc. Ocean Drill. Program Sci. Results*, *138*, 839–854.

Moore, M. I., and P. J. Thomson (1991), Impact of Jittered sampling on conventional spectral estimates, *J. Geophys. Res.*, *96*, 18,519–18,526.

Moran, K. (1997), Elastic property correction applied to leg 154 sediment, Ceara Rise, *Proc. Ocean Drill. Program Sci. Results*, *154*, 151–155.

Muller, R., and G. MacDonald (2000), *Ice Ages and Astronomical Causes*, Springer-Verlag, New York.

Neeman, B. (1993), Orbital tuning of paleoclimate records: A reassessment, *Rep. LBNL-39572*, Lawrence Berkeley Lab., Berkeley, Calif.

Nobes, D., S. Bloomer, J. Mienert, and F. Westall (1991), Milankovitch cycles and nonlinear response in the Quaternary record in the Atlantic sector of the Southern Oceans, *Proc. Ocean Drill. Program Sci. Results*, *114*, 551–576.

Odell, J. (1975), Error estimation in stratigraphic correlation, *Math. Geol.*, *7*, 167–182.

Oppo, D. W., J. McManus, and J. Cullen (1998), Abrupt climate events 500,000 to 340,000 years ago: Evidence from subpolar North Atlantic sediments, *Science*, *279*, 1335–1338.

Oppo, D. W., L. Keigwin, J. McManus, and J. Cullen (2001), Persistent suborbital climate variability in marine isotope stage 5 and Termination II, *Paleoceanography*, *16*, 280–292.

Pestiaux, P., and A. Berger (1984), Impacts of deep-sea processes on paleoclimatic spectra, in *Milankovitch and Climate, Part 1*, edited by A. Berger et al., pp. 493–510, D. Reidel, Norwell, Mass.

Petit, J., et al. (1999), CLimate and atmospheric history of the past 420,000 years from the Vostok ice core, Antarctica, *Nature*, *399*, 429–436.

Pisias, N. G., D. G. Martinson, T. Moore, N. J. Shackleton, W. Prell, J. Hays, and G. Boden (1984), High resolution stratigraphic correlation of benthic oxygen isotopic records spanning the last 300,000 years, *Mar. Geol.*, *56*, 119–136.

Prell, W. (1982), Oxygen and carbon isotope stratigraphy for the Quaternary of hole 502b: Evidence for two modes of isotopic variability, *Deep Sea Drill. Proj. Initial Rep.*, *68*, 455–464.

Prell, W., J. Imbrie, D. Martinson, J. Morley, N. Pisias, N. Shackleton, and H. Streeter (1986), Graphic correlation of oxygen isotope records: Application to the late Quaternary, *Paleoceanography*, *1*, 137–162.

Press, W., S. Teukolsky, W. Vetterling, and B. Flannery (1999), *Numerical Recipes in C*, Cambridge Univ. Press, New York.

Ravelo, A. C., and N. J. Shackleton (1995), Evolution of surface water circulation in the east equatorial Pacific over the past 2.0 Ma: Isotopic measurements from ODP Site 851, *Proc. Ocean Drill. Program Sci. Results*, *138*, 503–514.

Raymo, M. E. (1997), The timing of major climate terminations, *Paleoceanography*, *12*, 577–585.

Roe, G., and M. Allen (1999), A comparison of competing explanations for the 100,000-yr ice age cycle, *Geophys. Res. Lett.*, *26*, 2259–2262.

Rubincam, D. (1994), Insolation in terms of Earth's orbital parameters, *Theor. Appl. Climatol.*, *48*, 195–202.

Ruddiman, W. F., M. Raymo, D. Martinson, B. Clement, and J. Backman (1989), Pleistocene evolution: Northern Hemisphere ice sheets and the North Atlantic Ocean, *Paleoceanography*, *4*, 353–412.

Schrag, D., G. Hampt, and D. Murray (1996), Pore fluid constraints on the temperature and oxygen isotopic composition of the glacial ocean, *Science*, *272*, 1930–1932.

Schwarzacher, W. (1975), *Sedimentation Models and Quantitative Stratigraphy*, Elsevier Sci., New York.

Shackleton, N. J., and M. Hall (1984), Oxygen and carbon isotope stratigraphy of Deep Sea Drilling Project hole 552a: Plio-Pleistocene glacial history, *Deep Sea Drill. Proj. Initial Rep.*, *81*, 599–609.

Shackleton, N. J., and N. D. Opdyke (1972), Oxygen isotope and palaeomagnetic stratigraphy of equatorial Pacific core V28-238: Oxygen isotope temperature and ice volumes on a 10^5 and 10^6 year scale, *Quat. Res.*, *3*, 39–55.

Shackleton, N. J., and N. D. Opdyke (1976), Oxygen-isotope and paleomagnetic stratigraphy of Pacific core V28-239: Late Pliocene to latest Pleistocene, *Geol. Soc. Am. Bull.*, *145*, 449–464.

Shackleton, N. J., A. Berger, and W. R. Peltier (1990), An alternative astronomical calibration of the lower Pleistocene timescale based on ODP site 677, *Trans. R. Soc. Edinburgh Earth Sci.*, *81*, 251–261.

Shackleton, N. J., T. K. Hagelberg, and S. J. Crowhurst (1995), Evaluating the success of astronomical tuning: Pitfalls of using coherence as a criterion for assessing pre-Pleistocene timescales, *Paleoceanography*, *10*, 693–697.

Shaw, A. (1964), *Time in Stratigraphy*, McGraw-Hill, New York.

Singer, B., and M. Pringle (1996), Age and duration of the Matuyama-Brunhes geomagnetic polarity reversal from $^{40}Ar/^{39}Ar$ incremental analysis of lavas, *Earth Planet. Sci. Lett.*, *139*, 47–61.

Skinner, L., and I. McCave (2003), Analysis and modelling of gravity- and piston-coring based on soil mechanics, *Mar. Geol.*, *199*, 181–204.

Tauxe, L., T. Herbert, and N. Shackleton (1996), Astronomical calibration of the Matuyama Brunhes boundary: Consequences for magnetic remanence acquisition in marine carbonates and the asian loess sequences, *Earth Planet. Sci. Lett.*, *140*, 133–146.

Thierstein, H., K. Geitzenauer, B. Molfino, and N. Shackleton (1977), Global synchroneity of late Quaternary coccolith datum levels: Validation by oxygen isotopes, *Geology*, *5*, 400–404.

Thomson, D. (1990), Time series analysis of Holocene climate data, *Philos. Trans. R. Soc. London A*, *330*, 601–616.

Tiedemann, R., M. Sarnthein, and N. J. Shackleton (1994), Astronomic timescale for the Pliocene Atlantic $\delta^{18}O$ and dust flux records of ODP site 659, *Paleoceanography*, *9*, 619–638.

Venz, K., D. Hodell, C. Stanton, and D. Warnke (1999), A 1.0 Myr record of glacial North Atlantic intermediate water variability from ODP site 982 in the northeast Atlantic, *Paleoceanography*, *14*, 42–52.

von Storch, H., and F. W. Zwiers (1999), *Statistical Analysis in Climate Research*, Cambridge Univ. Press, New York.

Williams, D., R. Thunell, E. Tappa, D. Rio, and I. Raffi (1988), Chronology of the Pleistocene

oxygen isotope record: 0–1.88 m.y. BP, *Palaeogeogr. Palaeoclimatol. Palaeoecol.*, *64*, 221–240.

Winograd, I., T. Coplen, J. Landwehr, A. Riggs, K. Ludwig, B. Szabo, P. Kolesar, and K. Revesz (1992), Continuous 500,000-year climate record from vein calcite in Devils Hole, Nevada, *Science*, *258*, 255–260.

Winograd, I., J. Landwehr, K. Ludwig, T. Coplen, and A. Riggs (1997), Duration and structure of the past four interglacials, *Quat. Res.*, *48*, 141–154.

Wunsch, C. (1996), *The Ocean Circulation Inverse Problem*, Cambridge Univ. Press, New York.

Wunsch, C. (2000), On sharp spectral lines in the climate record and the millennial peak, *Paleoceanography*, *15*, 417–424.

Wunsch, C. (2003a), The spectral description of climate change including the 100 ky energy, *Clim. Dyn.*, *20*, 353–363.

Wunsch, C. (2003b), Determining the paleoceanographic circulations, with emphasis on the Last Glacial Maximum, *Quat. Sci. Rev.*, *22*, 371–385.

Yiou, P., C. Genthom, M. Ghil, J. Jouzel, J. Barnola, C. Lorius, and Y. Korotkevitch (1991), High-frequency paleovariability in climate and CO_2 levels from Vostok ice core records, *J. Geophys. Res.*, *96*, 20,365–20,378.

P. Huybers and C. Wunsch, Program in Atmospheres, Oceans, and Climate, Massachusetts Institute of Technology, Room 54-1724, Cambridge MA 02139, USA. (phuybers@mit.edu)